



UNIVERSITY OF LEEDS

This is a repository copy of *Metabolic control of BRISC–SHMT2 assembly regulates immune signalling*.

White Rose Research Online URL for this paper:  
<http://eprints.whiterose.ac.uk/147110/>

Version: Accepted Version

---

**Article:**

Walden, M, Tian, L, Ross, RL et al. (15 more authors) (2019) Metabolic control of BRISC–SHMT2 assembly regulates immune signalling. *Nature*, 570 (7760). pp. 194-199. ISSN 0028-0836

<https://doi.org/10.1038/s41586-019-1232-1>

---

(c) 2019, The Author(s), under exclusive licence to Springer Nature Limited. This is an author produced version of a paper published in *Nature*. Uploaded in accordance with the publisher's self-archiving policy.

**Reuse**

Items deposited in White Rose Research Online are protected by copyright, with all rights reserved unless indicated otherwise. They may be downloaded and/or printed for private study, or other acts as permitted by national copyright laws. The publisher or other rights holders may allow further reproduction and re-use of the full text version. This is indicated by the licence information on the White Rose Research Online record for the item.

**Takedown**

If you consider content in White Rose Research Online to be in breach of UK law, please notify us by emailing [eprints@whiterose.ac.uk](mailto:eprints@whiterose.ac.uk) including the URL of the record and the reason for the withdrawal request.



[eprints@whiterose.ac.uk](mailto:eprints@whiterose.ac.uk)  
<https://eprints.whiterose.ac.uk/>

# Metabolic control of BRISC-SHMT2 assembly regulates immune signaling

Miriam Walden<sup>1,9</sup>, Lei Tian<sup>2,9</sup>, Rebecca Ross<sup>3</sup>, Upasana M. Sykora<sup>1</sup>, Dominic P. Byrne<sup>4</sup>, Emma L. Hesketh<sup>1</sup>, Safi K. Masandi<sup>1</sup>, Joel Cassel<sup>5</sup>, Rachel George<sup>1</sup>, James R. Ault<sup>1</sup>, Farid El Oualid<sup>6</sup>, Krzysztof Pawłowski<sup>7,8</sup>, Joseph M. Salvino<sup>5</sup>, Patrick A. Eyers<sup>4</sup>, Neil A. Ranson<sup>1</sup>, Francesco Del Galdo<sup>3</sup>, Roger A. Greenberg<sup>2\*</sup> and Elton Zeqiraj<sup>1\*</sup>

<sup>1</sup>Astbury Centre for Structural Molecular Biology, School of Molecular and Cellular Biology, Faculty of Biological Sciences, Astbury Building, Room 8.109, University of Leeds, Leeds, LS2 9JT, UK

<sup>2</sup>Department of Cancer Biology, Basser Center for BRCA, Perelman School of Medicine, University of Pennsylvania, 421 Curie Blvd, Philadelphia, PA 19104-6160, US

<sup>3</sup>Leeds Institute of Rheumatic and Musculoskeletal Medicine, University of Leeds, Leeds, LS2 9JT, UK

<sup>4</sup>Department of Biochemistry, Institute of Integrative Biology, University of Liverpool, Crown St, Liverpool, L69 7ZB, UK

<sup>5</sup>The Wistar Cancer Center for Molecular Screening, The Wistar Institute, 3601 Spruce Street, Philadelphia, PA 19104-4265, US

<sup>6</sup>UbiQ Bio BV, Science Park 408, 1098 XH Amsterdam, The Netherlands

<sup>7</sup>Warsaw University of Life Sciences, ul. Nowoursynowska 166, 02-787 Warszawa, Poland

<sup>8</sup>Department of Translational Medicine, Clinical Sciences, Lund University, Lund, Sweden

<sup>9</sup>These authors contributed equally to this work

\*To whom correspondence may be addressed:

Elton Zeqiraj (email: [e.zeqiraj@leeds.ac.uk](mailto:e.zeqiraj@leeds.ac.uk); Tel: +44 113 3433079)

Roger A. Greenberg (email: [rogergr@penncmedicine.upenn.edu](mailto:rogergr@penncmedicine.upenn.edu); Tel: 215-746-2738)

## Summary

SHMT2 regulates one-carbon transfer reactions essential for amino acid and nucleotide metabolism, using PLP as a cofactor. Apo SHMT2 exists as a dimer with unknown functions, whereas PLP binding stabilizes the active, tetrameric state. SHMT2 also promotes inflammatory cytokine signaling by interacting with the BRISC deubiquitylase (DUB) complex, although it is unclear if this function relates to metabolism. We reveal the cryo-EM structure of human BRISC-SHMT2 complex at 3.8 Å resolution. The BRISC complex is a U-shaped dimer of four subunits and SHMT2 sterically blocks the BRCC36 active site and inhibits DUB activity. Only the inactive SHMT2 dimer, but not the active, PLP-bound tetramer binds and inhibits BRISC. BRISC mutations that disrupt SHMT2 binding impaired type I interferon signaling in response to inflammatory stimuli. Intracellular PLP levels regulated BRISC-SHMT2 interaction and inflammatory cytokine responses. These data reveal a new mechanism of metabolite regulation of DUB activity and inflammatory signaling.

Serine hydroxymethyltransferase 2 (SHMT2) functions in one-carbon folate metabolism supporting purine and thymine synthesis required for cell growth and proliferation. Full-length SHMT2 localizes to mitochondria via an N-terminal mitochondria-targeting sequence (MTS), whilst an N-terminal truncation (residues 1-21) generates the cytoplasmic SHMT2 $\alpha$  isoform<sup>1,2</sup> (**Fig. 1a**). Pyridoxal-5'-phosphate (PLP), the active form of vitamin B6, promotes a shift in SHMT2 oligomeric state from an inactive dimer to the enzymatically active tetramer<sup>1,3</sup>.

SHMT2 also controls inflammatory cytokine signaling via interaction with the deubiquitylating (DUB) enzyme BRISC (BRCC36 isopeptidase complex). BRCC36 is a JAMM/MPN<sup>+</sup> Zn<sup>2+</sup>-dependent DUB and functions within two macromolecular complexes, requiring interaction with MPN<sup>-</sup> pseudo-DUBs Abraxas1 or Abraxas2 for DUB activity<sup>4-6</sup> (**Fig. 1a**). The nuclear ARISC complex partners with RAP80 and BRCA1, forming the BRCA1-A complex required for DNA repair<sup>7-9</sup><sup>10</sup>. Direct interaction with SHMT2 enhances BRISC delivery to ubiquitylated type I interferon (IFN) receptors (IFNAR1/2)<sup>11,12</sup> allowing BRCC36 to deubiquitylate K63-Ub chains on IFNAR1/2, limiting their endocytosis and lysosomal degradation<sup>12</sup>. BRISC-deficient mice exhibit attenuated IFN responses and are protected from pathological conditions stemming from elevated inflammatory signaling<sup>12</sup>. BRISC-SHMT2 association therefore provides a potential link between metabolism and inflammation.

The BRCC36-Abraxas2 complex is an obligate dimer of heterodimers essential for DUB activity and IFN signaling<sup>13,14</sup>. Similarly, BRISC and ARISC complexes are active as stable dimers of tetramers with stoichiometry 2:2:2:2<sup>4,5,13,15</sup>. Structures of the human BRISC complex are unavailable and the molecular basis for SHMT2 binding and regulation is unknown. We present the cryo-EM structure of the BRISC-SHMT2 complex at 3.8 Å resolution revealing the BRISC complex architecture and the molecular basis for DUB activity inhibition by SHMT2. Structure-guided mutations or increasing intracellular PLP levels reduced BRISC-SHMT2 interaction and inflammatory signalling, revealing a direct link between vitamin B6 metabolism and control of immune responses.

### **SHMT2 is an endogenous BRISC inhibitor**

We produced SHMT2 $\Delta$ N (residues 18-504), which lacks the MTS and is a mixture of dimers and tetramers in solution (**Fig. 1b**). Tetramer peak fractions absorbed strongly at 435 nm indicating PLP association, consistent with previous findings that PLP binding promotes a shift from an inactive dimer to the active SHMT2 tetramer <sup>1</sup> (**Fig. 1c and Extended Data Fig. 1a, b**). Dimer and tetramer peaks were confirmed by native mass spectrometry (MS) (**Extended Data Fig. 1c**).

A serendipitous SHMT2 A285T mutation near the PLP acceptor Lys280 residue was identified by the Structural Genomics Consortium (PDBid 6DK3). SHMT2 $\Delta$ N+A285T is dimeric in solution and crystal lattice, allowing a direct comparison between dimer (apo enzyme) and tetramer (holoenzyme) structures (**Extended Data Fig. 1a-d**). Individual SHMT2 $\alpha$ -WT and SHMT2 $\Delta$ N+A285T protomer structures are similar, suggesting that the A285T mutation does not significantly perturb the structure (**Extended Data Fig. 1e**). However, the A285T mutation reduces covalent PLP association, subsequent tetramerization and catalytic activity (**Extended Data Fig. 2a, b**). PLP addition induced SHMT2 $\Delta$ N dimer-tetramer transition, leading to a large shift in thermal melting temperature (**Extended Data Fig. 2c, d**). This shift was largely reduced or abolished in A285T and K280A SHMT2 mutants, in agreement with studies showing SHMT2 mutations that abrogate PLP binding shift the equilibrium towards the dimer <sup>1,16-19</sup> (**Extended Data Fig. 2e**).

Addition of SHMT2 $\Delta$ N inhibited BRISC DUB activity (**Fig. 1d**). Dimeric SHMT2 $\Delta$ N was a better inhibitor ( $IC_{50}$  = 9 nM) than the tetrameric form ( $IC_{50}$  = 77.5 nM). As SHMT2 $\Delta$ N tetramer is not fully saturated with PLP (**Extended Data Fig. 2c, d**), preincubation with PLP further reduced BRISC inhibition by the SHMT2 $\Delta$ N tetramer (**Fig. 1d**). The obligate dimers SHMT2 $\Delta$ N+A285T and SHMT2 $\Delta$ N+K280A+A285T were effective inhibitors of BRISC and similar to SHMT2 $\Delta$ N dimers (**Fig. 1d**). SHMT2 $\Delta$ N+A285T DUB inhibition was selective for BRISC compared to ARISC (**Fig. 1e**), confirming that SHMT2 does not interact with the ARISC complex <sup>12</sup>. These data suggest a previously unknown role for the dimeric (PLP-free) form of SHMT2 in regulating BRISC DUB activity.

## BRISC-SHMT2 complex structure

To understand the molecular basis of BRISC-SHMT2 association and how PLP-dependent SHMT2 oligomerization affects DUB activity, we solved the structure of the BRISC complex bound to an SHMT2 dimer. Using limited proteolysis we identified a minimal complex termed BRISC $\Delta$ N $\Delta$ C (**Extended Data Fig. 3a, b**), containing BRCC36, BRCC45, MERIT40 $\Delta$ N (72-329) and Abraxas2 $\Delta$ C (1-267). BRISC and BRISC $\Delta$ N $\Delta$ C were active towards a fluorogenic K63-linked diUb substrate (**Extended Data Fig. 3c**), and were each inhibited by SHMT2 $\Delta$ N+A285T with similar IC<sub>50</sub> values (**Extended Data Fig. 3d**). SHMT2 $\Delta$ N+A285T formed a stable, equimolar complex with BRISC $\Delta$ N $\Delta$ C (**Extended Data Fig. 3e, f**).

We used negative stain electron microscopy (EM) and single particle cryo-EM to evaluate BRISC $\Delta$ N $\Delta$ C and BRISC $\Delta$ N $\Delta$ C-SHMT2 $\Delta$ N+A285T complexes. BRISC $\Delta$ N $\Delta$ C particles showed distinct U-shaped assemblies similar to those seen for the nuclear ARISC complex<sup>15</sup>. However, BRISC $\Delta$ N $\Delta$ C showed heterogeneity and flexibility of the “arm” regions (**Extended Data Fig. 4a**). The BRISC $\Delta$ N $\Delta$ C-SHMT2 $\Delta$ N+A285T complex was homogeneous, with SHMT2 $\Delta$ N+A285T bridging both arms of the U-shaped BRISC structure in 2D class averages (**Extended Data Fig. 4a**). We collected a large cryo-EM dataset, and identified ~11% (71,262 particles) with a structure with apparent C2 symmetry, containing a central trapezoid region and two extending arms. The remaining particles are missing one arm (**Extended Data Fig. 4b, c**). After 3D classification and refinement, using both C1 and C2 symmetry, we obtained EM density maps at 3.8 Å and 4.2 Å resolution respectively (**Extended Data Fig. 4c, d; Extended Data Table 1**).

BRISC $\Delta$ N $\Delta$ C complex comprises a central core region and two extending arms. Insect BRCC36-Abraxas2 structure (PDBid 5CW3)<sup>13</sup> was fitted at the base of the map, and the quality of the EM density in this region was sufficient for modeling the human BRCC36-Abraxas2 sequence into the structure (**Fig. 2**). The SHMT2 $\Delta$ N+A285T dimer was immediately recognizable in the EM map, with the structure (PDBid 6DK3) fitting directly above the BRCC36-Abraxas2 MPN domains (**Fig. 2**). The remaining unoccupied density belongs to BRCC45 and MERIT40, for which no experimental structures are available.

BRCC45 contains two UEV domains at its N- and C-termini. We used the FFAS03<sup>20</sup> and HHpred<sup>21</sup> algorithms to search for additional domains and identified a putative “UBC-like” domain within residues 144-280, suggesting the presence of a middle UEV domain (UEV-M). Tandemly repeated domains are common during protein evolution, reinforcing the independent prediction of a third UEV domain in BRCC45 (**Fig. 1a**)<sup>22</sup>. Consistent with this hypothesis, we manually built a C $\alpha$ -backbone structure for two consecutive UEV domains of BRCC45 into the density immediately extending from Abraxas2 (**Fig. 2a**). However, due to the low resolution of this region, precise assignment of the sequence was not possible.

We used the related ARISC complex structure<sup>15</sup> as a guide to place homology models of MERIT40 and a third UEV (BRCC45) domain within the “fist”-like density in the distal region of each arm (**Fig. 2a**). The resolution in this peripheral region is poor (~10 Å), so it was not possible to ascertain the precise orientation of the vWFA (MERIT40) and UEV-C (BRCC45) domains. We modelled UEV-N and UEV-C in proximity of Abraxas2 and MERIT40 (respectively), in accordance with previous deletion studies<sup>4,23</sup> (**Fig. 2a**). Thus, a complete BRISC-SHMT2 model was built using a combination of known structures, *de novo* model building and homology modeling (**Fig. 2a**). The “core” structure consisting of the BRCC36-Abraxas2 superdimer and the SHMT2 obligate dimer are well resolved with local resolution of 3.5-4.0 Å (**Extended Data Fig. 4c, d and 5a, b**).

SHMT2 bridges the two arms of the BRISC complex and sits directly above the BRCC36-Abraxas2 superdimer, explaining the requirement for superdimer formation in SHMT2 binding<sup>13</sup>. SHMT2 interacts with MPN domains of BRCC36 and Abraxas2 and UEV-N and UEV-M of BRCC45 (**Fig. 2a**). The main BRISC-interacting surface on SHMT2 is centered on the two  $\alpha$ 6 helices, and proximal residues between SHMT2-Abraxas2, SHMT2-BRCC36 and Abraxas2-BRCC45 are shown in **Fig. 2b**. MERIT40 does not contact SHMT2 directly (**Fig. 2a**) and its position may provide stabilizing interactions to BRCC45, while also interacting with other signaling molecules<sup>24</sup>. Comparison between human and insect BRCC36-Abraxas2 superdimers reveals a similar overall structure, with minor local shifts (**Extended Data Fig. 5c-e**). Overall, the structure provides the first view of the interaction surfaces between SHMT2 and components of the BRISC complex.

Prior work suggested that BRISC also interacts with SHMT1 in cells, although cellular BRISC-SHMT2 complexes were much more abundant <sup>12</sup>. To test if SHMT2 and SHMT1 interact equally with BRISC *in vitro*, we purified SHMT1 dimers and tetramers, but failed to assemble BRISC-SHMT1 complexes, and observed no inhibition of BRISC DUB activity *in vitro* (**Extended Data Fig. 6**). While it remains possible that BRISC-SHMT1 complexes form in cells, we predict these will be lower affinity in comparison with BRISC-SHMT2 complexes and may be a consequence of indirect interactions with other factors.

We mutated SHMT2 residues in proximity to BRISC (**Fig. 2b**) and assessed their effects on DUB activity *in vitro*. Mutations were made in the SHMT2 $\Delta$ N+A285T background, which purifies as a dimer (**Extended Data Fig. 7a, b**). SHMT2 $\Delta$ N+A285T containing L211R or L215R were each less potent inhibitors of BRISC DUB activity when compared to SHMT2 $\Delta$ N+A285T, while the L211R+L215R mutant had no detectable inhibitory effect on BRISC activity (**Extended Data Fig. 7c**). SHMT2 $\Delta$ N inhibition was also observed with hexaUb chains as substrates (**Extended Data Fig. 7d**). DUB activity was only marginally reduced when assayed with SHMT2 $\Delta$ N+A285T+L211R+L215R, SHMT2 $\Delta$ N tetramers or SHMT1, mirroring results obtained with fluorescently labeled diUb, and consistent with the observation that L211R+L215R mutations reduce BRISC-SHMT2 interaction *in vitro* (**Extended Data Fig. 8a**). These experiments establish SHMT2 helix  $\alpha$ 6 as the most important contact surface for BRISC interaction and DUB activity inhibition.

### **BRISC-SHMT2 impacts immune signaling**

To understand the relevance of the BRISC-SHMT2 interaction in cells, we mutated interface residues between SHMT2, Abraxas2 and BRCC45 (**Fig. 2b**) and assessed interactions by co-immunoprecipitation (**Fig. 3a, b**). Consistent with the loss of interaction with SHMT2, Abraxas2 mutants A142R, E144A and E144R expressed in Abraxas2<sup>-/-</sup> MEFs showed reduced STAT1 phosphorylation in response to HSV infection, as did N100R, Y107R and D23R mutants, which either reduce or prevent BRCC45-MERIT40 binding (**Fig. 3c**). The BRISC-SHMT2 interaction was also required for immune signaling when cells were challenged using LPS or IFN $\beta$  (**Fig. 3d**). Moreover, we observed



increased IFNAR1 ubiquitylation after IFN stimulation of cells overexpressing the Abraxas2 E144R mutant (**Extended Data Fig. 7e**).

For a broader view of immune signaling output dependent on the BRISC-SHMT2 complex, we performed qRT-PCR analysis of 79 genes commonly upregulated during a type I interferon response. Ectopic expression of WT-Abraxas2 resulted in 48 genes upregulated between 2-8,000 fold in response to LPS (**Fig. 3e and Extended Data 9a**). Accordingly, LPS challenging of Abraxas2<sup>-/-</sup> (KO) cells or KO + Abraxas2 E144R cells showed a poor response, with 11 and 8 genes (respectively) upregulated 2-10 fold compared to non-challenged KO cells (**Fig. 3e**).

We next mutated SHMT2 residues to ascertain their importance in cellular assembly of BRISC-SHMT2 complexes. Overexpression of SHMT2 $\Delta$ N+L211R+L215R resulted in loss of BRISC-SHMT2 interaction in MEF cells, mirroring the results seen *in vitro* (**Extended Data Fig. 7f and 8a**). pSTAT1 levels were also affected in cells challenged with LPS (**Extended Data Fig. 7g**), and we observed increased IFNAR1 ubiquitylation after IFN stimulation of cells overexpressing the SHMT2 $\Delta$ N+L211R+L215R mutant (**Extended Data Fig. 7e**). Collectively, these findings reveal the specific Abraxas2 and SHMT2 surfaces that are required for BRISC-SHMT2 complex assembly and immune signaling in cells.

The positioning of SHMT2 within the structure provides a potential rationale for its inhibition of DUB activity since it blocks the BRCC36 active site (**Extended Data Fig. 8b**). Kinetic data suggests SHMT2 acts as an apparent competitive inhibitor (**Extended Data Fig. 8c**). However, the increase in  $K_m$  was only moderate (~2-fold at equimolar BRISC-SHMT2 complex), suggesting that K63-Ub chains might displace bound SHMT2 from BRISC when poly-ubiquitylated substrates are in close proximity. This model would account for the counterintuitive function of SHMT2 as both an inhibitor of BRISC activity and an essential mediator of BRISC association with sites of DUB action (**Extended Data Fig. 10**). It is also possible that other factors and post-translational modifications trigger SHMT2 dissociation from BRISC in cells. We propose that SHMT2 acts as a reversible

endogenous BRISC inhibitor that prevents non-specific DUB activity. This regulated safety mechanism is similar in concept to protease inhibition by endogenous inhibitors<sup>25</sup>. To our knowledge, SHMT2 is the first example of an endogenous DUB inhibitor, acting as a precedent for the possible regulation of other DUBs *in vivo*.

### **Regulation of BRISC-SHMT2 interaction by PLP**

BRISC DUB inhibition provides the first non-enzymatic role of the SHMT2 dimer. Our structure explains why the apo SHMT2 dimer, but not the PLP-bound tetramer inhibits DUB activity. SHMT2 helix  $\alpha 6$  interacts with BRISC which overlaps with the SHMT2 tetramerization surface, accounting for the observation that SHMT2 tetramer and the BRISC-SHMT2 complexes are mutually exclusive (**Extended Data Fig. 1b and 8d**). The SHMT2 $\Delta$ N-PLP tetramer does not form BRISC-SHMT2 complexes *in vitro* (**Extended Data Fig. 8e**), suggesting that PLP-induced tetramerization could regulate SHMT2 dimer availability, and BRISC-SHMT2 complex formation in cells.

To test this hypothesis, we cultured MEF and 293T cells in B6 vitamer-free media and compared the BRISC-SHMT2 interaction after pyridoxal (PL) supplementation (**Fig. 4a**). PLP levels were confirmed by vitamin B6 metabolite measurements in whole cell lysates (**Fig. 4b**), and fewer SHMT2 dimers are present after PL supplementation (**Extended Data Fig. 9b**). This coincided with a marked reduction of overexpressed SHMT2 $\Delta$ N and endogenous Abraxas2 interaction (**Fig. 4a**). Similarly, the interaction between overexpressed Abraxas2 and endogenous SHMT2 was reduced (**Fig. 4c**). The PLP-dependent reduction of BRISC-SHMT2 interaction was not observed when PLP-resistant SHMT2 mutants were expressed (**Fig. 4d**).

We next measured pSTAT1 levels and observed a PL-dependent reduction of pSTAT1 upon IFN $\beta$  stimulation (**Fig. 4e and Extended Data Fig. 9c**). This reduction was not observed when PLP-resistant SHMT2 mutants were expressed (**Fig. 4e, Extended Data Fig. 9d**). Consistently, we observed an increase in both BRISC-SHMT2 complexes (**Fig. 4d and Extended Data 9e**) and pSTAT1 levels when PLP-resistant SHMT2 mutants were

expressed in cells cultured in B6 vitamer-containing media and challenged with IFN $\beta$  or HSV (**Fig. 4e**, **Extended Data Fig. 9d, f**). Finally, we observed a PLP-dependent reduction of nine IFN-induced genes in LPS-challenged MEFs that stably express SHMT2 $\Delta$ N, but saw no change in MEFs where a PLP-resistant mutant was expressed (**Fig. 4f**). Interestingly, IL10 was upregulated by 2.1-fold in PL<sup>+</sup> SHMT2 $\Delta$ N cells (**Fig. 4f**), although this was not upregulated in LPS-stimulated Abraxas2 cells, suggesting that IL10 is not directly dependent on BRISC-SHMT2 (**Extended Data 9a**). These experiments provide further evidence that PLP binding to SHMT2 regulates BRISC-SHMT2 interaction and immune signaling in cells.

Endogenous small molecule ligands that control ubiquitin signaling could be physiologically important. PLP influence on BRISC activity establishes a regulatory precedent for DUBs, akin to the plant hormone auxin and the second messenger inositol hexakisphosphate, which both allosterically regulate the activity of E3 ubiquitin ligases <sup>26</sup>. Post-translational modifications of the PLP acceptor lysine <sup>27,28</sup> could provide additional layers of regulation for BRISC-SHMT2 association and immune signaling. It is possible that natural and synthetic SHMT2 binders, such as folate and PLP analogues, can modulate dimeric SHMT2 availability or conformation and thus interferon signaling (**Extended Data Fig. 10**). Understanding the regulatory mechanisms of BRISC-SHMT2 interactions will therefore be useful to unlock the potential for such molecules as therapeutics.

## Data availability

Coordinates were deposited in the Protein Data Bank: PDBid 6R8F. Cryo-EM reconstructions in C1 and C2 were deposited in the EM Data Bank: EMD-4759 and EMD-4760.

## Author Contribution

M.W. performed EM experiments, data processing and model building with assistance from E.L.H. and S.K.M.; L.T. performed cell based experiments, immunoprecipitation, challenge assays, metabolic analysis and immunoblots; M.W. and U.M.S. cloned and purified proteins and performed *in vitro* interaction studies; R.R. and F.D.G. performed qRT-PCR and gene expression data analysis; D.B. and P.A.E. performed DSF assays and data analysis; J.C. performed enzyme kinetics; R.G. and J.R.A. performed mass spectrometry analyses; F.E.O. generated reagents; K.P. performed bioinformatics analyses; J.S., P.A.E., F.D.G., N.A.R. and R.A.G. contributed to conception and supervision of experiments; E.Z. performed enzyme assays and conceived and supervised the project; E.Z., M.W., L.T., R.A.G. wrote the manuscript with input from N.A.R., P.A.E. and F.D.G.; all authors critically reviewed the manuscript.

## Acknowledgments

We thank Frank Sicheri, Juan Fontana, Alan Berry, Celeste Simon, Itzhak Nissim, Frank Sobott, Joseph Cockburn and Alex Moloney for useful discussions and Rebecca Thompson, Alice Gordon, Matthew Iadanza and Martin Fuller for technical support. Supported by a Sir Henry Dale Fellowship (Wellcome Trust and the Royal Society; 200523/Z/16/Z) to E.Z., MRC MC\_PC-16050 grant to E.Z. and F.D.G., NIH R01 CA138835 and a Lupus Research Alliance Target Identification in Lupus grant to R.A.G and J.M.S., a BBSRC (BB/L021250/1) grant to N.A.R, a BBSRC TDRF grant BB/N021703/1 and North West Cancer Research grants CR1088, CR1097 to P. A.E., and a Polish National Science Centre grant (2014/15/B/NZ1/03359) to K.P. University of Leeds mass spectrometry facility was supported by BBSRC (BB/E012558/1) and Wellcome Trust (208385/Z/17/Z) grants.

The Astbury cryo-EM facility is funded by a University of Leeds ABSL award and Wellcome Trust grant 108466/Z/15/Z.

## Competing Interests

F.E.O. declares competing financial interests as co-founder and shareholder of UbiQ Bio BV.

## Materials and Methods

### Cloning, protein expression and purification of BRISC-SHMT2 complex and SHMT1

Genes for the four-subunit human BRISC complex were cloned in the MultiBac system used for co-expression of multiprotein complexes in insect cells (*Sf9*)<sup>29</sup>. A single 6-His purification tag followed by a cleavable TEV site was engineered at the N-terminus of BRCC45. Virus preparation, protein production and protein purification were performed as previously described by Zeqiraj et al., 2015<sup>13</sup>.

Wild-type and mutant forms of human SHMT2 $\Delta$ N (residues 18-504) and SHMT1 were cloned in a pProEx-HTb vector and expressed in *E. coli* BL21 (DE3) codon plus RIL in Terrific Broth (TB) in the presence of 100  $\mu$ g/ml Ampicillin and 34  $\mu$ g/ml Chloramphenicol at 37 °C to an OD<sub>600</sub> of 1.0-1.2 AU. Cells were then induced with 0.5 mM isopropyl-1-thio-D-galactopyranoside (IPTG) and incubated overnight at 18 °C. Cells were harvested by centrifugation at 5,500g and cell pellets were resuspended in lysis buffer (50 mM Tris-HCl, pH 7.6, 300 mM NaCl, 20 mM imidazole, 0.075%  $\beta$ -mercaptoethanol, 5% glycerol, 1 mM Benzamidine, 0.8 mM phenylmethyl sulfonyl fluoride (PMSF) and 0.3 mg/ml lysozyme). Cells were lysed by sonication (1 sec on, 3 sec off for a total of 16 min) on ice and the lysates were cleared by centrifugation at 26,000g. The clarified lysate was loaded onto a 5 ml chelating FastFlow column (GE Healthcare), charged with Ni<sup>2+</sup>. The column was washed with 4 column volumes (CV) of wash buffer consisting of 50 mM Tris-HCl (pH 7.6), 500 mM NaCl, 20 mM imidazole, 0.075%  $\beta$ -mercaptoethanol and 1 mM Benzamidine, and the protein was eluted by applying an imidazole gradient with elution buffer consisting of 50 mM Tris-HCl (pH 7.6), 300 mM NaCl, 300 mM imidazole, 0.075%  $\beta$ -mercaptoethanol and 1 mM Benzamidine. The fractions containing SHMT2 $\Delta$ N or SHMT1 were pooled and

dialyzed against buffer containing 20 mM MES, pH 6.5, 250 mM NaCl, 5% glycerol, 20 mM imidazole, 0.075%  $\beta$ -mercaptoethanol and 1 mM Benzamidine. TEV was added to the protein sample and incubated overnight at 4 °C. Dialyzed protein was loaded on a 16/600 Superdex200 column (GE Healthcare), equilibrated with 20 mM MES (pH 6.5), 500 mM NaCl and 2 mM TECP.

BRISC $\Delta$ N $\Delta$ C and SHMT2 $\Delta$ N+A285T were mixed in vitro at 1:4 molar ratio and incubated on ice for 40 min. The mixture was then injected onto a Superdex 10/300 S200 column and peak fractions were analysed by SDS-PAGE. Fractions containing the BRISC $\Delta$ N $\Delta$ C-SHMT2 $\Delta$ N+A285T complex were pooled and BRISC-SHMT2 $\Delta$ N+A285T complex was used immediately for grid preparation and EM analysis as described below. The remainder BRISC-SHMT2 $\Delta$ N+A285T complex was pooled and stored at -80 °C at a final concentration of 0.5 mg/ml. Denatured and native masses of all protein preparations were verified by mass spectrometry.

### **Negative stain EM**

BRISC $\Delta$ N $\Delta$ C and BRISC $\Delta$ N $\Delta$ C-SHMT2 $\Delta$ N+A285T complexes were diluted in buffer (25 mM Hepes, pH 7.5, 150 mM NaCl, 1 mM TCEP) to 0.0041 mg/ml and 0.0051 mg/ml respectively, immediately prior to grid preparation. Glow-discharged, 300-mesh carbon-coated copper grids (Agar scientific) were incubated with 7  $\mu$ l BRISC $\Delta$ N $\Delta$ C or BRISC $\Delta$ N $\Delta$ C-SHMT2 $\Delta$ N+A285T for 60 sec, passed through 3 droplets of water and stained twice with 2% w/v uranyl acetate for 20 sec and 10 sec respectively. Excess liquid was removed by blotting. Micrographs were collected on an FEI Tecnai F20 electron microscope operated at 120 kV equipped with an FEI Ceta CMOS camera. Data processing was carried out using RELION 2.1. Initially, ~1,500 particles were picked manually and extracted with a 450 Å<sup>2</sup> box size. Particles were subjected to reference-free 2D classification to generate initial references for auto-picking. A total of 28,566 and 26,824 particles were picked for the BRISC $\Delta$ N $\Delta$ C and BRISC $\Delta$ N $\Delta$ C-SHMT2 $\Delta$ N+A285T complexes respectively. One round of reference-free 2D classification was then carried out for each.

## Cryo-grid preparation and data collection

BRIS $\Delta$ N $\Delta$ C-SHMT2 $\Delta$ N+A285T complex was diluted to 0.05 mg/ml in buffer (25 mM Hepes, pH 7.5, 150 mM NaCl, 1 mM TCEP) immediately prior to grid preparation. Cryo-EM grids were prepared by placing 3  $\mu$ l of this complex onto glow-discharged, 200-mesh copper grids (Quantifoil R1.2/1.3), followed by immediate blotting and plunge-freezing in liquid ethane cooled by liquid nitrogen, using an FEI Vitrobot IV at 95 % relative humidity, chamber temperature of 4 °C. Datasets were collected on an FEI Titan Krios transmission electron microscope at 300 kV, using a total electron dose between 83-95 e<sup>-</sup>/Å<sup>2</sup>, a magnification of 75,000x and a final calibrated object sampling of 1.065 Å/pixel. Three independent datasets giving a total of 7,494 movies were recorded using the EPU automated acquisition software on an FEI Falcon III direct electron detector<sup>30</sup>. Each exposure movie had a total exposure time of 2 sec collected over 70-79 frames with an electron dose of 1.2 e<sup>-</sup>/Å<sup>2</sup> per frame. Detailed information on data collection is shown in **Extended Data Table 1**.

## Image processing

A schematic of the data processing pipeline is shown in **Extended Data Fig. 4**. Image processing was carried out using RELION 3.0<sup>31</sup>. Drift-corrected averages of each movie were created using MOTIONCORR2<sup>32</sup> and the contrast transfer function of each determined using gCTF<sup>33</sup>. Initially, ~ 2,000 particles for each dataset were manually picked, extracted with a box size of 373 Å<sup>2</sup> and subjected to reference-free 2D classification to generate initial references for auto-picking. After auto-picking, each dataset was individually subjected to iterative rounds of reference-free 2D classification. Based on visual inspection, quality 2D average classes were selected for each dataset and then the three sets were combined. An initial model generated *ab initio* from the 2D class averages of the BRIS $\Delta$ N $\Delta$ C-SHMT2 negative stain data, filtered to ~60 Å, was used for initial 3D classification of the combined dataset. Of the eight classes generated, one contained particles comprising the intact complex, i.e. the BRCC36-Abraxas2-SHMT2 core and both BRCC45-MERIT40 arms. This class was processed as a separate dataset consisting of 71,262 particles, representing the complete, 2-arm structure. In parallel, this class along with four others, totalling 514,930 particles, was processed to represent the complete dataset. Both were subjected to a final round of 3D classification to remove any

remaining 'bad' particles. The best classes from 3D classification were taken forward and subjected to 3D refinement, per-particle CTF correction and particle polishing<sup>31</sup>. C2 symmetry was imposed to the 2-arm dataset. Post-processing was used to appropriately mask the model, estimate and correct for the B-factor of the maps. Final resolutions were determined using the 'gold standard' Fourier shell correlation criterion (FSC = 0.143). Local resolution was estimated using the local resolution feature in RELION.

### **Model building and refinement**

A preliminary model for the BRISC $\Delta$ N $\Delta$ C-SHMT2 $\Delta$ N+A285T complex was generated using a combination of known crystal structures [BRCC36-Abraxas2 superdimer from *Camponotus floridanus* (PDBid 5CW3) and human SHMT2 dimer (PDBid 6DK3)] and homology models generated by Phyre2<sup>34</sup> (BRCC45, consisting of two UEV domains, and MERIT40). This initial model was manually fitted into the EM density map for the C1 reconstruction (3.8 Å) using rigid body fitting in UCSF Chimera<sup>35</sup>. The model was then manually fitted and rebuilt in COOT<sup>36</sup> to trace the human sequences of BRCC36 and Abraxas2. Amino acid residues which lacked unambiguous density were deleted or modelled up to their C $\beta$  position while preserving sequence information. The C $\alpha$ -backbone for BRCC45 UEV-N and -M was traced into the remaining density mainly as alanine and glycine residues and the precise sequence for BRCC45 could not be modelled with confidence. Gaps numbered arbitrarily were left where direct connectivity between secondary structure elements could not be determined.

The higher resolution C1 map was used for initial model building and the 2-arm model was generated by using the two-fold symmetry of the superdimer core.

The model was refined against the C1 and C2 maps in Phenix<sup>37</sup> using default parameters and secondary structure restraints. The overall quality of the model was assessed using MolProbity<sup>38</sup>. Fitting of the remaining BRCC45 UEV-C and MERIT40 domains into the peripheral parts of the C2 EM map was carried out using rigid body fitting in Chimera and these are displayed for relative position and size comparison purposes only.

### **DUB activity assays**



BRISC complexes were assayed at 30 °C in DUB reaction buffer containing 50 mM HEPES-NaOH pH 7.0, 100 mM NaCl, 0.1 mg/ml BSA, 1 mM DTT and 0.005% Tween-20. Internally quenched fluorescent (IQF) K63-linked diUb (Lifesensors, catalog number: DU6303) was used as a reporter for DUB activity [1 part IQF diUB : 9 parts unlabelled K63-linked diUb prepared as described by Pickart and Raasi 2005<sup>39</sup>]. 20- $\mu$ l enzyme reactions were carried out in 384-well black flat-bottom low flange plates (Corning; 35373). Cleaved diUb was monitored by measuring fluorescence intensity (Ex 540 nm, Em. 580 nm; dichroic mirror 560 nm) every 1 min over 20 min, and initial velocity ( $v_0$ ) was calculated as the slope of the linear part of the reaction progress curve. Fluorescence intensity units were converted to nM product concentration using TAMRA-labelled ubiquitin (Lifesensors, catalog number: SI270T) as a standard. Enzyme concentrations for which a reasonable progress curve was obtained over 20 min were: 1 nM BRISC and 40 nM ARISC. Substrate concentration was 300 nM. IC<sub>50</sub> values were calculated by fitting the data using the GraphPad Prism built-in dose-response equation for inhibition with variable slope:  $Y = \text{Bottom} + (\text{Top} - \text{Bottom}) / (1 + 10^{((\text{Log}IC_{50} - X) * h)})$ . Michaelis-Menten analysis in the absence and presence of increasing concentrations of SHMT2 were performed in DUB buffer containing 50 mM HEPES-NaOH (pH 6.8), 100 mM NaCl and 5 mM DTT. BRISC concentration was 1.5-2.0 nM and IQF K63-linked diUb was used (0-4  $\mu$ M) as substrate (concentrations greater than 4  $\mu$ M inhibited BRISC activity). Data were fit using the standard Michaelis-Menten equation, constraining  $V_{\text{max}}$  to be less than the  $V_{\text{max}}$  in the absence of SHMT2. Lineweaver-Burk plots and Michaelis-Menten analysis were performed using GraphPad Prism.

K63-linked hexaUb chains were also used to determine DUB activity. 60  $\mu$ l reactions were carried out in 1.5 ml Eppendorfs at 30 °C in DUB reaction buffer. BRISC was incubated in the presence or absence of SHMT2 $\Delta$ N or SHMT1 forms for 30 mins at room temperature prior to K63-Ub<sub>6</sub> addition. Reactions containing 0.5 nM BRISC, 2  $\mu$ M SHMT, 1  $\mu$ M K63-Ub<sub>6</sub> were incubated for 1 hour. Immunoblotting was performed with commercially available HRP-conjugated antibody to Ub (P4D1, Santa Cruz).

### **SHMT2 PLP association and enzyme activity assays**

PLP association assays were performed in 20  $\mu$ l reactions in 384-well plates (Greiner) in buffer containing 50 mM HEPES-Na (pH 7.8), 50 mM NaCl, 50 mM KCl, 5% glycerol, 0.2 mM DTT, 0.1 mM EDTA and 0.005% Tween-20. SHMT2 $\Delta$ N and point mutants (5  $\mu$ M) were rapidly mixed with PLP (100  $\mu$ M) and the reaction was monitored by measuring absorbance at 435 nm (every 30 sec over 1 hour) using a Hidex Sense microplate reader. SHMT2 $\Delta$ N enzyme activity was monitored in 20  $\mu$ l reactions in 384-well, UV-transparent plates (Greiner). The synthetic substrate L-threo-phenylserine (2S,3R)-2-amino-3-hydroxy-3-phenylpropionic acid (BACHEM) was used as described previously<sup>40</sup> with minor modifications. Reactions were performed in buffer containing 50 mM HEPES-Na (pH 7.5), 100 mM NaCl, 0.5 mM TCEP and 0.005% Tween-20. SHMT2 $\Delta$ N and point mutants (2  $\mu$ M) were preincubated with 200  $\mu$ M PLP for 1 hour at 25 °C. 5  $\mu$ l of enzyme-PLP solution was added to 15  $\mu$ l of solution containing 0-260 mM L-threo-phenylserine and the reaction was monitored by measuring absorbance of benzaldehyde at 279 nm in a Hidex Sense microplate reader (every 2 min over 20 min). Absorbance units were converted to molar concentrations using a standard curve of known concentrations of benzaldehyde solutions (Sigma). Initial velocity ( $v_0$ ) was calculated as the slope of the linear part of the reaction progress curve (20 min).

### **Differential scanning fluorimetry (DSF)**

Thermal-shift assays were performed using an Applied Biosystems StepOnePlus Real-Time PCR instrument and a standardized DSF procedure<sup>41</sup>. Proteins were diluted in 50 mM Tris-HCl (pH 7.4) and 100 mM NaCl to a concentration of 5  $\mu$ M and then incubated with the indicated concentration of compound in a total reaction volume of 10  $\mu$ L, with final concentration of 2% (v/v) DMSO. SYPRO Orange (Invitrogen) was used as a fluorescence probe. The temperature was raised in regular 0.3 °C intervals from 25 °C to 95 °C. Compound binding experiments were assessed in duplicate and reported relative to DMSO controls. Normalized data were processed using the Boltzmann equation to generate sigmoidal denaturation curves, and  $T_m/\Delta T_m$  values were calculated as previously described<sup>41</sup>.

### **Native mass spectrometry (MS)**

BRISC $\Delta$ N $\Delta$ C-SHMT2 $\Delta$ N+A285T (2.6  $\mu$ M) and SHMT2 $\Delta$ N and various mutants (2-20  $\mu$ M) were buffer exchanged into 0.2-1 M ammonium acetate (pH 7.2) using Zeba Spin 7K MWCO desalting columns (ThermoFisher). Samples were analysed by nanoelectrospray ionisation MS using either a quadrupole-IMS-orthogonal time-of-flight (TOF) MS (Synapt HDMS, Waters UK Ltd., Manchester, UK), operated as described previously <sup>42</sup> or a quadrupole orbitrap MS modified for transmission of high m/z ions (Q-Exactive Plus, ThermoScientific), operated as described previously <sup>43,44</sup>. Both used gold/palladium coated nanospray tips prepared in-house. Data from the Synapt was processed using the MassLynx v4.1 suite of software supplied with the mass spectrometer and UniDec v2.7.1 <sup>45</sup>. Data from the Q-Exactive Plus was processed using Xcalibur Qual Browser v4.0.27.19 and UniDec v2.7.1.

### **Analytical size exclusion chromatography**

BRISC-FL and SHMT2 $\Delta$ N or SHMT1 forms were mixed *in vitro* at 1:1 molar ratio (~6  $\mu$ M) and incubated on ice for 30 min. The mixture was then injected onto a 2.4 ml Superose 6 analytical size exclusion column. Peak fractions were analysed by SDS-PAGE. Controls for each protein were also run.

### **Immunoprecipitation and immunoblots**

All immunoprecipitations were performed as previously described <sup>46</sup>. Briefly, BRCC36 and Abraxas2 expressing cells were lysed in NETN 150 (0.5% NP40, 25 mM Tris pH 7.5, 150 mM NaCl, 0.5 mM EDTA with 1mM PMSF). Flag-IPs were performed on lysate supernatants for 4 hours with agarose conjugated anti-Flag M2 beads (Sigma) prior to elution in 0.1 mM glycine (pH 2.5). Immunoblots were performed with the following rabbit polyclonal antibodies at 1:1000 dilution that were generated to recombinant proteins: MERIT40, Abraxas2, BRCC36 and BRCC45. Commercially available antibodies to HA epitope (HA.11 Covance) and SHMT2 (Cell Signaling) were used according to the manufacturer's directions. An Abraxas2 deletion mutant (DM1) was used as control as described previously <sup>12</sup>.

For assessment of IFNAR1 ubiquitylation in cells, cells were lysed in buffer containing 2% SDS, 150 mM NaCl, 10 mM Tris-HCl, pH 8.0, 50 mM sodium fluoride, 10mM N-

Ethylmaleimide and protease inhibitors. After boiling for 10 mins, cell lysates were further diluted in immunoprecipitation buffer (10 mM Tris-HCl, pH 8.0, 150 mM NaCl, 2 mM EDTA, 1% Triton). IFNAR1 were immunoprecipitated with a corresponding antibody (Bethyl Laboratories A304-290A). Resulting samples were separated by SDS-PAGE and analyzed by immunoblotting using the anti-ubiquitin antibody (Lifesensor, VU101).

### **Response to HSV infection, LPS, and IFN- $\beta$**

HSV lacking the ICP0 gene was used to infect cells at a multiplicity of infection of 0.1 for 2 hours. Media was then changed followed by a 5-hour incubation period. Cells were then lysed in NETN150 and lysates were run on a 4-12% gradient SDS-PAGE gel for immunoblot. Phospho-STAT1 and STAT1 antibodies were purchased from Cell Signaling Corporation and used according to the manufacturer's specifications. Monitoring of phospho-STAT1 after LPS or IFN- $\beta$  treatment was performed using similar conditions as described previously <sup>12</sup>.

### **Cellular PLP level manipulation and validation**

MEF or 293T cells were cultured in B6 vitamer-free Dulbecco's modified eagle's medium (DMEM, from Gibco), B6 vitamer-free DMEM + 20  $\mu$ mol/L pyridoxal hydrochloride (PL, from Sigma) or B6 vitamer-free DMEM+ 50  $\mu$ mol/L PL. All media were supplemented with 10% FBS. After 48 hours culture, cells were collected and snap frozen in liquid nitrogen. Pyridoxal, pyridoxal phosphate, and pyridoxine levels was measured using LC/MS as described previously <sup>47</sup>.

### **qRT-PCR analysis of gene expression in MEFs**

IFN type I-related gene expression was analysed in *Abraxas2*<sup>-/-</sup> MEFs following treatment with either LPS or vehicle control. Gene expression was performed in *Abraxas2*<sup>-/-</sup> MEFs and compared to derivative lines that had been stably reconstituted with *Abraxas2* WT or mutant E144R using retroviral transduction. Following 16 hours of LPS exposure, cells were directly lysed in TRIzol™ (Thermo Fisher Scientific, Waltham, MA) and RNA extracted using Quick-RNA Miniprep Kit (Zymo Research, Irvine, CA) as per manufacturer's instructions. 400 ng of eluted RNA was converted to cDNA using RT2 First

Strand Kit (Qiagen). Next, the cDNA was mixed with RT2 SYBR Green Mastermix (Qiagen, Venlo, Netherlands). The mouse IFN I RT2 Profiler PCR Array (Qiagen cat. no. PAMM-016Z) was performed and relative expression determined using the  $\Delta\Delta\text{CT}$  method and normalized for 4 housekeeping genes according to manufacturer's guidance. Single measurements of three biological repeats were performed. Total results were analysed and compared to *Abraxas2*<sup>-/-</sup> MEFs gene signature, with and without LPS treatment. Gene expression analysis of MEFs cultured in vitamer-free B6 with and without 20  $\mu\text{M}$  PL was performed as above.

## References

1. Giardina, G., Brunotti, P., Fiascarelli, A., Cicalini, A., Costa, M. G. S., Buckle, A. M., di Salvo, M. L., Giorgi, A., Marani, M., Paone, A., Rinaldo, S., Paiardini, A., Contestabile, R. & Cutruzzolà, F. How pyridoxal 5'-phosphate differentially regulates human cytosolic and mitochondrial serine hydroxymethyltransferase oligomeric state. *FEBS Journal* **282**, 1225–1241 (2015).
2. Anderson, D. D., Woeller, C. F., Chiang, E.-P., Shane, B. & Stover, P. J. Serine hydroxymethyltransferase anchors de novo thymidylate synthesis pathway to nuclear lamina for DNA synthesis. *J Biol Chem* **287**, 7051–7062 (2012).
3. Szebenyi, D. M., Liu, X., Kriksunov, I. A., Stover, P. J. & Thiel, D. J. Structure of a murine cytoplasmic serine hydroxymethyltransferase quinonoid ternary complex: evidence for asymmetric obligate dimers. *Biochemistry* **39**, 13313–13323 (2000).
4. Patterson-Fortin, J., Shao, G., Bretscher, H., Messick, T. E. & Greenberg, R. A. Differential Regulation of JAMM Domain Deubiquitinating Enzyme Activity within the RAP80 Complex. *J Biol Chem* **285**, 30971–30981 (2010).
5. Cooper, E. M., Boeke, J. D. & Cohen, R. E. Specificity of the BRISC deubiquitinating enzyme is not due to selective binding to Lys63-linked polyubiquitin. *J Biol Chem* **285**, 10344–10352 (2010).
6. Feng, L., Wang, J. & Chen, J. The Lys63-specific deubiquitinating enzyme BRCC36 is regulated by two scaffold proteins localizing in different subcellular compartments. *J Biol Chem* **285**, 30982–30988 (2010).
7. Sobhian, B., Shao, G., Lilli, D. R., Culhane, A. C., Moreau, L. A., Xia, B., Livingston, D. M. & Greenberg, R. A. RAP80 targets BRCA1 to specific ubiquitin structures at DNA damage sites. *Science* **316**, 1198–1202 (2007).
8. Abraxas and RAP80 form a BRCA1 protein complex required for the DNA damage response. **316**, 1194–1198 (2007).
9. Kim, H., Chen, J. & Yu, X. Ubiquitin-binding protein RAP80 mediates BRCA1-dependent DNA damage response. *Science* **316**, 1202–1205 (2007).

10. Jiang, Q., Paramasivam, M., Aressy, B., Wu, J., Bellani, M., Tong, W., Seidman, M. M. & Greenberg, R. A. MERIT40 cooperates with BRCA2 to resolve DNA interstrand cross-links. *Genes Dev* **29**, 1955–1968 (2015).
11. Sowa, M. E., Bennett, E. J., Gygi, S. P. & Harper, J. W. Defining the human deubiquitinating enzyme interaction landscape. *Cell* **138**, 389–403 (2009).
12. Zheng, H., Gupta, V., Patterson-Fortin, J., Bhattacharya, S., Katlinski, K., Wu, J., Varghese, B., Carbone, C. J., Aressy, B., Fuchs, S. Y. & Greenberg, R. A. A BRISC-SHMT Complex Deubiquitinates IFNAR1 and Regulates Interferon Responses. *CellReports* **5**, 180–193 (2013).
13. Zeqiraj, E., Tian, L., Piggott, C. A., Pillon, M. C., Duffy, N. M., Ceccarelli, D. F., Keszei, A. F. A., Lorenzen, K., Kurinov, I., Orlicky, S., Gish, G. D., Heck, A. J. R., Guarné, A., Greenberg, R. A. & Sicheri, F. Higher-Order Assembly of BRCC36-KIAA0157 Is Required for DUB Activity and Biological Function. *Mol. Cell* **59**, 970–983 (2015).
14. Walden, M., Masandi, S. K., Pawłowski, K. & Zeqiraj, E. Pseudo-DUBs as allosteric activators and molecular scaffolds of protein complexes. *Biochem. Soc. Trans.* **46**, BST20160268–466 (2018).
15. Kyrieleis, O. J. P., McIntosh, P. B., Webb, S. R., Calder, L. J., Lloyd, J., Patel, N. A., Martin, S. R., Robinson, C. V., Rosenthal, P. B. & Smerdon, S. J. Three-Dimensional Architecture of the Human BRCA1-A Histone Deubiquitinase Core Complex. *CellReports* **17**, 3099–3106 (2016).
16. Zanetti, K. A. & Stover, P. J. Pyridoxal phosphate inhibits dynamic subunit interchange among serine hydroxymethyltransferase tetramers. *J Biol Chem* **278**, 10142–10149 (2003).
17. Jagath, J. R., Sharma, B., Rao, N. A. & Savithri, H. S. The Role of His-134, -147, and -150 Residues in Subunit Assembly, Cofactor Binding, and Catalysis of Sheep Liver Cytosolic Serine Hydroxymethyltransferase. *J Biol Chem* **272**, 24355–24362 (1997).
18. Jala, V. R., Appaji Rao, N. & Savithri, H. S. Identification of amino acid residues, essential for maintaining the tetrameric structure of sheep liver cytosolic serine

- hydroxymethyltransferase, by targeted mutagenesis. *Biochem J* **369**, 469–476 (2003).
19. Krishna Rao, J. V., Jagath, J. R., Sharma, B., Appaji Rao, N. & Savithri, H. S. Asp-89: a critical residue in maintaining the oligomeric structure of sheep liver cytosolic serine hydroxymethyltransferase. *Biochem J* **343 Pt 1**, 257–263 (1999).
  20. Xu, D., Jaroszewski, L., Li, Z. & Godzik, A. FFAS-3D: improving fold recognition by including optimized structural features and template re-ranking. *Bioinformatics* **30**, 660–667 (2014).
  21. Zimmermann, L., Stephens, A., Nam, S.-Z., Rau, D., Kübler, J., Lozajic, M., Gabler, F., Söding, J., Lupas, A. N. & Alva, V. A Completely Reimplemented MPI Bioinformatics Toolkit with a New HHpred Server at its Core. *J Mol Biol* **430**, 2237–2243 (2018).
  22. Björklund, A. K., Ekman, D. & Elofsson, A. Expansion of protein domain repeats. *PLoS Comput. Biol.* **2**, e114 (2006).
  23. Hu, X., Kim, J. A., Castillo, A., Huang, M., Liu, J. & Wang, B. NBA1/MERIT40 and BRE interaction is required for the integrity of two distinct deubiquitinating enzyme BRCC36-containing complexes. *J Biol Chem* **286**, 11734–11745 (2011).
  24. Guettler, S., LaRose, J., Petsalaki, E., Gish, G., Scotter, A., Pawson, T., Rottapel, R. & Sicheri, F. Structural basis and sequence rules for substrate recognition by Tankyrase explain the basis for cherubism disease. *Cell* **147**, 1340–1354 (2011).
  25. Hamilton, G., Colbert, J. D., Schuettelkopf, A. W. & Watts, C. Cystatin F is a cathepsin C-directed protease inhibitor regulated by proteolysis. *EMBO J* **27**, 499–508 (2008).
  26. Zheng, N. & Shabek, N. Ubiquitin Ligases: Structure, Function, and Regulation. *Annu. Rev. Biochem.* **86**, 129–157 (2017).
  27. Yang, X., Wang, Z., Li, X., Liu, B., Liu, M., Liu, L., Chen, S., Ren, M., Wang, Y., Yu, M., Wang, B., Zou, J., Zhu, W.-G., Yin, Y., Gu, W. & Luo, J. SHMT2 Desuccinylation by SIRT5 Drives Cancer Cell Proliferation. *Cancer Res.* **78**, 372–386 (2018).
  28. Cao, J., Sun, L., Aramsangtienchai, P., Spiegelman, N. A., Zhang, X., Huang, W., Seto, E. & Lin, H. HDAC11 regulates type I interferon signaling through defatty-



- acylation of SHMT2. *Proceedings of the National Academy of Sciences* **7**, 201815365–6 (2019).
29. Fitzgerald, D. J., Berger, P., Schaffitzel, C., Yamada, K., Richmond, T. J. & Berger, I. Protein complex expression by using multigene baculoviral vectors. *Nature Methods* **2006 3:12** **3**, 1021–1032 (2006).
  30. Thompson, R. F., Iadanza, M. G., Hesketh, E. L., Rawson, S. & Ranson, N. A. Collection, pre-processing and on-the-fly analysis of data for high-resolution, single-particle cryo-electron microscopy. *Nat Protoc* **14**, 100–118 (2018).
  31. Zivanov, J., Nakane, T., Forsberg, B. O., Kimanius, D., Hagen, W. J., Lindahl, E. & Scheres, S. H. New tools for automated high-resolution cryo-EM structure determination in RELION-3. *Elife* **7**, 163 (2018).
  32. Zheng, S. Q., Palovcak, E., Armache, J.-P., Verba, K. A., Cheng, Y. & Agard, D. A. MotionCor2: anisotropic correction of beam-induced motion for improved cryo-electron microscopy. *Nature Methods* **2006 3:12** **14**, 331–332 (2017).
  33. Zhang, K. Gctf: Real-time CTF determination and correction. *JOURNAL OF STRUCTURAL BIOLOGY* **193**, 1–12 (2016).
  34. Kelley, L. A., Mezulis, S., Yates, C. M., Wass, M. N. & Sternberg, M. J. E. The Phyre2 web portal for protein modeling, prediction and analysis. *Nat Protoc* **10**, 845–858 (2015).
  35. Pettersen, E. F., Goddard, T. D., Huang, C. C., Couch, G. S., Greenblatt, D. M., Meng, E. C. & Ferrin, T. E. UCSF Chimera--a visualization system for exploratory research and analysis. *J. Comput. Chem.* **25**, 1605–1612 (2004).
  36. Emsley, P., Lohkamp, B., Scott, W. G. & Cowtan, K. Features and development of Coot. *Acta Crystallogr D Biol Crystallogr* **66**, 486–501 (2010).
  37. Adams, P. D., Afonine, P. V., Bunkoczi, G., Chen, V. B., Davis, I. W., Echols, N., Headd, J. J., Hung, L. W., Kapral, G. J., Grosse-Kunstleve, R. W., McCoy, A. J., Moriarty, N. W., Oeffner, R., Read, R. J., Richardson, D. C., Richardson, J. S., Terwilliger, T. C. & Zwart, P. H. PHENIX: a comprehensive Python-based system for macromolecular structure solution. *Acta Crystallogr D Biol Crystallogr* **66**, 213–221 (2010).

38. Chen, V. B., Arendall, W. B., Headd, J. J., Keedy, D. A., Immormino, R. M., Kapral, G. J., Murray, L. W., Richardson, J. S. & Richardson, D. C. MolProbity: all-atom structure validation for macromolecular crystallography. *Acta Crystallogr D Biol Crystallogr* **66**, 12–21 (2010).
39. Pickart, C. M. & Raasi, S. *Methods in Enzymology*. **399**, 21–36 (Elsevier, 2005).
40. Wei, Z., Song, J., Wang, G., Cui, X., Zheng, J., Tang, Y., Chen, X., Li, J., Cui, L., Liu, C.-Y. & Yu, W. Deacetylation of serine hydroxymethyl-transferase 2 by SIRT3 promotes colorectal carcinogenesis. *Nat Comms* **9**, 1–16 (2018).
41. Byrne, D. P., Vonderach, M., Ferries, S., Brownridge, P. J., Eyers, C. E. & Eyers, P. A. cAMP-dependent protein kinase (PKA) complexes probed by complementary differential scanning fluorimetry and ion mobility–mass spectrometry. *Biochem J* **473**, 3159–3175 (2016).
42. Scarff, C. A., Almeida, B., Fraga, J., Macedo-Ribeiro, S., Radford, S. E. & Ashcroft, A. E. Examination of Ataxin-3 (atx-3) Aggregation by Structural Mass Spectrometry Techniques: A Rationale for Expedited Aggregation upon Polyglutamine (polyQ) Expansion. *Mol. Cell Proteomics* **14**, 1241–1253 (2015).
43. Gault, J., Donlan, J. A. C., Liko, I., Hopper, J. T. S., Gupta, K., Housden, N. G., Struwe, W. B., Marty, M. T., Mize, T., Bechara, C., Zhu, Y., Wu, B., Kleanthous, C., Belov, M., Damoc, E., Makarov, A. & Robinson, C. V. High-resolution mass spectrometry of small molecules bound to membrane proteins. *Nature Methods* **2006 3:12** **13**, 333–336 (2016).
44. Rose, R. J., Damoc, E., Denisov, E., Makarov, A. & Heck, A. J. R. High-sensitivity Orbitrap mass analysis of intact macromolecular assemblies. *Nature Methods* **2006 3:12** **9**, 1084–1086 (2012).
45. Marty, M. T., Baldwin, A. J., Marklund, E. G., Hochberg, G. K. A., Benesch, J. L. P. & Robinson, C. V. Bayesian Deconvolution of Mass and Ion Mobility Spectra: From Binary Interactions to Polydisperse Ensembles. *Anal. Chem.* **87**, 4370–4376 (2015).
46. Shao, G., Patterson-Fortin, J., Messick, T. E., Feng, D., Shanbhag, N., Wang, Y. & Greenberg, R. A. MERIT40 controls BRCA1-Rap80 complex integrity and recruitment to DNA double-strand breaks. *Genes Dev* **23**, 740–754 (2009).

47. Ochocki, J. D., Khare, S., Hess, M., Ackerman, D., Qiu, B., Daisak, J. I., Worth, A. J., Lin, N., Lee, P., Xie, H., Li, B., Wubbenhorst, B., Maguire, T. G., Nathanson, K. L., Alwine, J. C., Blair, I. A., Nissim, I., Keith, B. & Simon, M. C. Arginase 2 Suppresses Renal Carcinoma Progression via Biosynthetic Cofactor Pyridoxal Phosphate Depletion and Increased Polyamine Toxicity. *Cell Metabolism* **27**, 1263–1280.e6 (2018).

## Figure Legends

### Figure 1. SHMT2 dimer inhibits BRISC DUB activity

- a)** Domain architecture of SHMT2 and BRCC36-containing complexes. MTS = mitochondria-targeting sequence, SHMT = serine hydroxymethyltransferase, MPN = Mpr1/Pad1 N-terminal, CC = coiled coil, UEV = Ubiquitin E2 variant, vWFA = von Willebrand factor type A.
- b)** SHMT2 $\Delta$ N elution profile after size exclusion chromatography, monitored by measuring  $A_{280}$ . SHMT2 $\Delta$ N bound to pyridoxal-5'-phosphate (PLP) was detected by measuring  $A_{435}$ . Data are representative of three independent experiments.
- c)** Schematic of SHMT2 $\Delta$ N dimer-tetramer equilibrium in response to PLP binding.
- d)** BRISC DUB activity against a fluorogenic K63-linked diUb substrate in the presence of SHMT2 $\Delta$ N forms.
- e)** BRISC and ARISC DUB activity against a fluorogenic K63-linked diUb substrate in the presence of SHMT2 $\Delta$ N+A285T. Data in *d*, *e* are average  $\pm$  SEM of three independent experiments carried out in duplicate.

### Figure 2. Structure of the BRISC-SHMT2 complex

- a)** Cryo-EM density at contour level of 0.055 (C2 map) shown in transparent surface. Proteins are depicted as cartoon models. Due to low resolution in the extended “arm” regions, UEV-C (BRCC45) and vWFA (MERIT40) models are shown for size comparison only. **b)** Close-up view of BRISC-SHMT2 interfaces. Residues labeled in red were mutated in validation analysis.

### Figure 3. BRISC-SHMT2 interaction is important for interferon signaling

- a & b)** Immunoprecipitation (IP) was performed using anti-Flag antibody in 293T cells transiently transfected with Flag-HA epitope-tagged Abraxas2 wild-type (WT) or mutants. Immunoblotting was performed for the indicated proteins.
- c)** Abraxas2<sup>-/-</sup> MEFs and Abraxas2<sup>-/-</sup> MEFs stably reconstituted with WT or mutants were infected with Herpes Simplex Virus (HSV) lacking the lytic phase gene ICP0. IFN signalling was assessed by immunoblotting for STAT1 phosphorylated at Y701 (pSTAT1).
- d)** WT MEFs overexpressing Abraxas2 WT or E144R were challenged with LPS and IFN $\beta$ . IFN signaling was assessed as in *c*. Data in *a-d* are representative of three independent experiments. For gel source data, see Supplementary Figure 1.
- e)** Volcano plots illustrating the fold change in gene expression of IFN type I-stimulated genes relative to Abraxas2<sup>-/-</sup> KO MEFs without LPS treatment. p-values were calculated using a Student's t-test (two-tail distribution and equal variances between the two samples) on the triplicate

$2^{(-\Delta CT)}$  values for each gene in each treatment group compared to the control group. Genes below the  $p=0.05$  threshold were upregulated in WT+LPS, but represented as below statistical significance due to the relative expression in KO samples being almost zero. Regulated genes are highlighted in Extended Data Fig. 9a.

#### **Figure 4. PLP regulation of BRISC-SHMT2 interaction and signaling**

**a)** Immunoprecipitation (IP) of stably expressed Flag-HA epitope-tagged SHMT2 $\Delta$ N using an anti-Flag antibody. Immunoblotting was performed after pyridoxal (PL) treatment for 48 h. **b)** GC-MS measurements of B6 vitamers from whole cell lysates after culturing for 48 h in B6 vitamer-free media with and without PL. PLP = pyridoxal-5'-phosphate; PN = pyridoxine. **c)** IP of ectopically expressed Abraxas2 using an anti-Flag antibody in MEFs grown in B6 vitamer-free media for 48 h. Immunoblotting was performed for the indicated proteins after 20  $\mu$ M PL addition and/or 500 units/mL mouse IFN $\beta$ . **d)** IP using an anti-Flag antibody in MEFs stably expressing Flag-HA epitope-tagged SHMT2 forms. Immunoblotting was performed after treatment with 20  $\mu$ M PL for 48 h. **e)** pSTAT1 levels in MEFs stably expressing SHMT2 forms and cultured in B6 vitamer-free media. Cells were treated with 20  $\mu$ M PL and/or 500units/ml IFN $\beta$  for 48h. Data in a, c-e are representative of three independent experiments. For gel source data, see Supplementary Figure 1. **f)** Volcano plots comparing type I IFN-induced gene expression in MEFs stimulated with LPS and cultured in the absence (PL $^-$ ) or presence (PL $^+$ ) of 20  $\mu$ M PL. p-values were calculated using a Student's t-test (two-tail distribution and equal variances between the two samples) on the triplicate  $2^{(-\Delta CT)}$  values for each gene in each treatment group compared to the control group.

## Extended Data Figure Legends

### Extended Data Figure 1. SHMT2 exists in a dimer-tetramer equilibrium

**a)** Structure of SHMT2 $\Delta$ N+A285T dimer (PDBid 6DK3). Unbiased electron density maps are coloured green. The structure was erroneously deposited by the Structural Genomics Consortium (SGC) as wild type with PDBid 3OU5. It was corrected and redeposited with PDBid 6DK3 on 28 May 2018. **b)** Structure of wild type (WT) SHMT2 $\alpha$  tetramer (PDBid 4PVF) bound to pyridoxal-5'-phosphate (PLP). Regions in red show structural rearrangements upon PLP binding. **c)** Native mass spectrometry spectra (single measurement experiment) of SHMT2 $\Delta$ N forms (top) and measured and calculated masses (bottom). Calculated masses nearest to the measured masses are underlined. **d)** Size exclusion chromatography profiles of SHMT2 $\Delta$ N forms (top) and a Coomassie-stained SDS-PAGE gel (bottom). Data are representative of three independent experiments. **e)** Comparison of SHMT2 protomers with and without PLP.

### Extended Data Figure 2. PLP regulates SHMT2 dimer-tetramer transition

**a)** PLP association to the indicated SHMT2 $\Delta$ N forms. SHMT2-PLP internal aldimine linkage was monitored by measuring absorbance at 435 nm after rapid mixing of SHMT2 $\Delta$ N (5  $\mu$ M) and PLP (100  $\mu$ M). Data are average  $\pm$  SEM of four independent reactions.

**b)** Enzyme activity of the indicated SHMT2 $\Delta$ N forms (0.5  $\mu$ M) against the synthetic substrate L-threo-phenylserine in the presence of 50  $\mu$ M PLP. Reaction was monitored by measuring benzaldehyde absorbance at 279 nm. Data are average  $\pm$  SEM of three independent experiments carried out in duplicate.

**c)** Differential scanning fluorimetry (DSF) analysis of SHMT2 $\Delta$ N forms in the presence and absence of PLP. SHMT2 $\Delta$ N WT and mutant proteins (5  $\mu$ M) were incubated with the indicated concentrations of PLP or 100  $\mu$ M 2-Hydroxy-6-methylpyridine-3-carboxylic acid (HMCA) for 10 min at 20  $^{\circ}$ C prior to DSF analysis.

**d)** Changes in melting temperatures ( $\Delta T_m$ ) for each of the conditions shown in **c**.  $\Delta T_m$  was calculated by subtracting the  $T_m$  of SHMT2 with buffer without ligands from the  $T_m$  of SHMT2 with added ligands. Data in **c**, **d** represent a single experiment carried out in duplicate.

**e)** Summary of SHMT2 $\Delta$ N+A285T dimer-tetramer equilibrium in response to PLP binding.

### Extended Data Figure 3. Reconstitution of BRISC-SHMT2 complex

**a)** Summary of limited proteolysis and Edman sequencing results indicating trypsin protease-labile regions for the BRCC45-MERIT40 complex (left) and the BRISC complex (right). Protease cleavage sites are shown as scissors. Unstructured Abraxas2 regions are indicated as dashed lines. MPN = Mpr1/Pad1 N-terminal, CC = coiled coil, UEV = Ubiquitin E2 variant, vWFA = von Willebrand factor type

A. **b)** SDS-PAGE of BRISC and BRISC $\Delta$ N $\Delta$ C complexes (representative of three independent experiments). **c)** DUB activity of BRISC (full length) and BRISC $\Delta$ N $\Delta$ C (truncated) complexes against a fluorogenic K63-linked diUb substrate. Data are average  $\pm$ SEM of three independent experiments carried out in duplicate. **d)** SHMT2 $\Delta$ N+A285T inhibition of BRISC and BRISC $\Delta$ N $\Delta$ C DUB activity. Data are average  $\pm$ SEM of three independent experiments carried out in duplicate. 95% confidence intervals are shown in square brackets. **e)** Size exclusion chromatography of the BRISC $\Delta$ N $\Delta$ C-SHMT2 $\Delta$ N+A285T complex (top) and Coomassie-stained SDS-PAGE of peak fractions (bottom). **f)** Native mass spectrometry of the BRISC $\Delta$ N $\Delta$ C-SHMT2 $\Delta$ N+A285T complex. Data in *e*, *f* are representative of three independent experiments.

#### **Extended Data Figure 4. Electron microscopy (EM) analysis of BRISC and BRISC-SHMT2 complexes**

**a)** Negative stain EM analysis. Selected 2D averaged classes of BRISC $\Delta$ N $\Delta$ C (left) and BRISC $\Delta$ N $\Delta$ C-SHMT2 $\Delta$ N+A285T (right).  
**b)** Representative cryo-EM micrograph. Green circles (180 Å diameter) indicate auto-picked particles.  
**c)** Flowchart of data processing. Final electron microscopy maps colored according to local resolution are provided (scale bar in Å). **d)** Fourier Shell Correlation (FSC) curves for the indicated maps. The final resolution was calculated using the “gold-standard” FSC cut-off at 0.143 frequency.

#### **Extended Data Figure 5. Structural analysis of BRISC-SHMT2 structures**

**a)** Structural overview of the BRISC $\Delta$ N $\Delta$ C-SHMT2 structure and cryo-EM maps at a contour level of 0.085 (C2 map), showing secondary structure features. BRCC45 UEV-C and MERIT40 vWFA domains were omitted. CCHB = coiled coil helical bundle. Asterisks mark the position of BRCC36 active site. An overreaching loop (SHMT2 residues 296-307) is coloured red. **b)** Representative EM map of BRCC36 active site. **c & d)** Superdimer BRCC36-Abraxas2 structures of human (**c**) and insect (*C. floridanus*) (**d**) highlighting differences and similarities. Connectivity of the MPN<sup>-</sup> domain of Abraxas2 and helix  $\alpha$ 4 by a crossover loop is different in the human complex and is colored orange. **e)** Superimposition of the BRCC36 MPN<sup>+</sup> domain from the insect (gray) and human (blue, green) heterodimers. Abraxas2 regions with notable differences between the two structures are colored orange.

#### **Extended Data Figure 6. Analysis of SHMT1 interaction with BRISC**

**a)** Elution profile of WT-SHMT1 from an S75 16/600 size exclusion chromatography column (data are representative of two independent experiments).  
**b)** Elution profile of SHMT1 containing mutated residues designed to break the tetrameric interface (left panel; data are from a single experiment). Structure of SHMT1 tetramer (PDBid 1RV4) highlighting residues important for tetramerization (right panel).

**c)** BRISC DUB activity against a fluorogenic K63-linked diUb substrate in the presence of the indicated SHMT1 and SHMT2 forms. Data are average  $\pm$ -SEM of three independent experiments carried out in duplicate. For gel source data, see Supplementary Figure 1.

**d)** Coomassie-stained SDS-PAGE analysis of the indicated SHMT1 and SHMT2 protein preparations (data are from a single experiment).

**e)** Analytical size exclusion chromatography runs of the indicated protein preparations. SHMT1 proteins were mixed with BRISC for 30 min before injecting on a 2.4 ml Superose 6 column (bottom traces). Traces on top are control runs. A BRISC-SHMT2 $\Delta$ N run is shown as reference (see Extended Fig. **8e** for detailed analysis).

**f)** Coomassie-stained SDS-PAGE analysis of the indicated peak fractions from size exclusion runs shown in panel **e**. Data in **e**, **f** are from a single experiment.

#### **Extended Data Figure 7. Purification and analysis of SHMT2 mutants**

**a)** Elution profile of the indicated SHMT2 $\Delta$ N forms from an S75 10/300 size exclusion chromatography column (single experiment). **b)** Coomassie-stained SDS-PAGE analysis of the indicated SHMT2 $\Delta$ N protein preparations (data are representative of two independent experiments). **c)** BRISC DUB activity against a fluorogenic K63-linked diUb substrate in the presence of the indicated SHMT2 $\Delta$ N mutants. Data are average  $\pm$ -SEM of three independent experiments carried out in duplicate. **d)** BRISC DUB activity against K63-linked hexa-Ub chains in the presence of the SHMT2 $\Delta$ N or SHMT1 forms. **e)** Ubiquitylation levels of IFNAR1 after IFN $\alpha$  stimulation in 293T cells overexpressing the indicated Abraxas2 and SHMT2 $\Delta$ N forms (LL->RR = L211R+L215R). IFNAR1 immunoprecipitation (IP) was performed under denaturing conditions and ubiquitin levels were detected using the vu-1 antibody. Mock IP was performed using a generic rabbit IgG antibody. **f)** Immunoprecipitation (IP) performed using anti-Flag antibody in MEFs transiently transfected with Flag-HA epitope-tagged SHMT2 $\Delta$ N or mutants. Immunoblot was performed for Abraxas2 and SHMT2 as indicated. UTF = untransfected cells used as control. **g)** MEFs overexpressing the indicated SHMT2 $\Delta$ N or mutants were challenged with LPS and interferon receptor-dependent signal transduction response was assessed by immunoblot for STAT1 phosphorylated at Y701 (pSTAT1). Data shown in **d-e** are representative of three independent experiments. For gel source data, see Supplementary Figure 1.

#### **Extended Data Figure 8. SHMT2 blocks the BRISC active site**

**a)** Analytical size exclusion chromatography (SEC) of SHMT2 $\Delta$ N forms preincubated with BRISC (left) and SDS-PAGE analysis of peak fractions (right). Data are from a single experiment. **b)** K63-linked diUb (gray) modeled on the MPN<sup>+</sup> domain of BRCC36 using the AMSH-LP-diUb structure (PDBid 2ZNV) as a guide. SHMT2 obligate dimer sterically clashes with the modeled proximal ubiquitin. **c)** Michaelis-Menten (top) and Lineweaver-Burk (bottom) plots for BRISC DUB activity against a K63-diUb



fluorogenic substrate with addition of SHMT2 $\Delta$ N+A285T. Technical duplicates are shown and data are representative of two independent experiments. **d)** Superimposition of SHMT2 dimer and tetramer forms. SHMT2 obligate dimer from the PLP-bound tetramer structure (PDBid 4PVF, colored gray) was overlaid to the SHMT2 $\Delta$ N+A285T dimer bound to BRISC. The second obligate dimer from the SHMT2-PLP holoenzyme sterically clashes with the BRCC36-Abraxas2 superdimer. Movement of helices  $\alpha$ 6 and  $\alpha$ 7 is indicated. **e)** Analytical SEC of SHMT2 $\Delta$ N dimer and tetramer (+PLP) forms with BRISC (left) and SDS-PAGE analysis of peak fractions (right). Data are from a single experiment.

### **Extended Data Figure 9. Regulation of BRISC-SHMT2 function in cells**

**a)** Schematic of pairwise comparison of Abraxas2<sup>-/-</sup> MEFs treated with LPS and expressing the indicated Abraxas2 forms (top panel). Bar chart illustrates the IFN type I-related genes that were >2 fold increased in Abraxas2 WT+LPS (black) and Abraxas2 E144R+LPS (blue) relative to KO+LPS. Data are presented as mean +/- SEM from three independent experiments (biological replicates).

**b)** Native gel electrophoresis of whole MEF cell lysates cultured in B6 vitamer-free media with and without pyridoxal (PL) and expressing the indicated Flag-HA-SHMT2 $\Delta$ N forms.

**c & d)** Measurement of pSTAT1 levels (pY701) in MEFs (**c**) or MEFs stably expressing SHMT2 (**d**) and cultured in B6 vitamer-free media. Where indicated, cells were treated with 20  $\mu$ M PL and/or or 500 units/mL IFN $\beta$  for 48 h.

**e)** IP performed using anti-Flag antibody in MEFs transiently transfected with Flag-HA epitope-tagged SHMT2 or mutants (cultured in DMEM). Immunoblot was performed for Abraxas2 and SHMT2 as indicated.

**f)** pSTAT1 levels (pY701) measured in MEFs cultured in DMEM containing B6 and the indicated SHMT2 forms after challenging with HSV. Data shown in *b-f* are representative of three independent experiments. For gel source data, see Supplementary Figure 1.

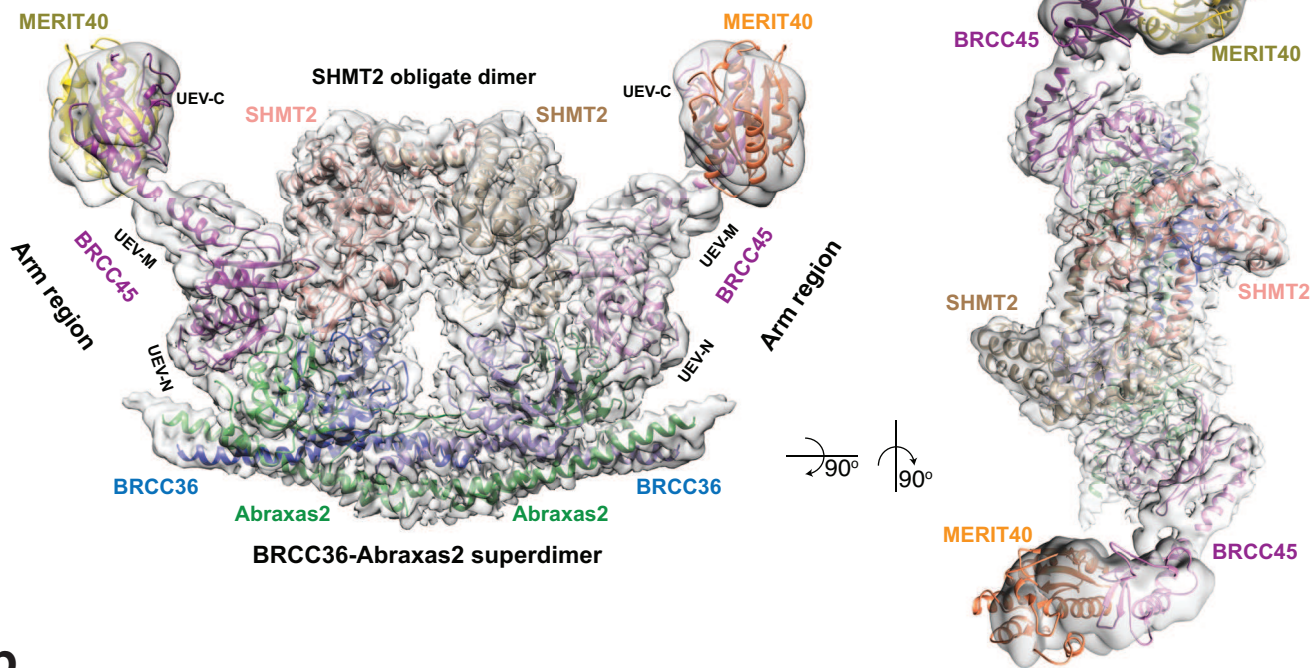
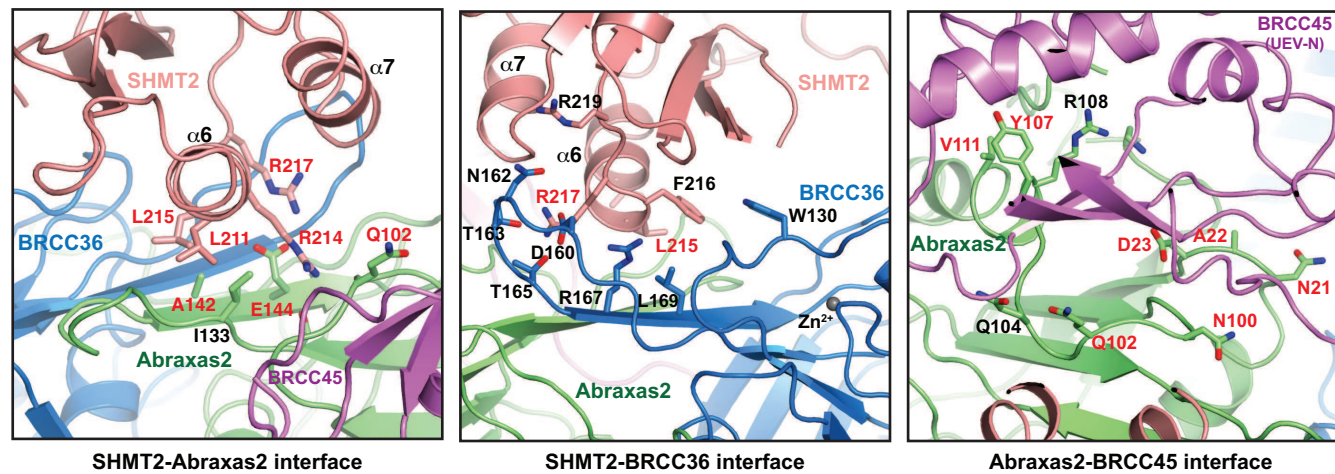
### **Extended Data Figure 10. Proposed model of BRISC-SHMT2 regulation of cytokine signaling**

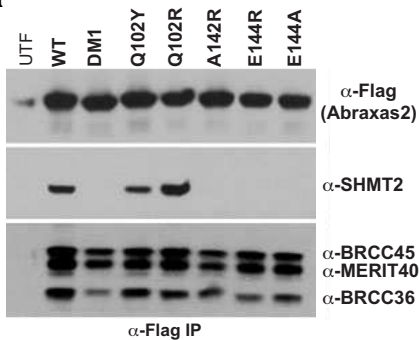
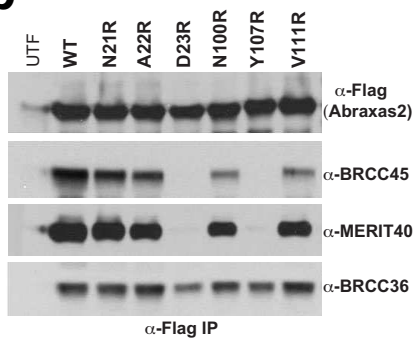
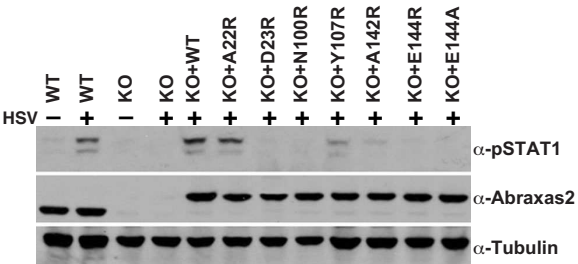
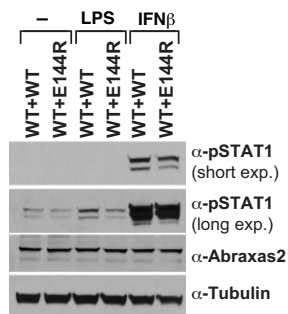
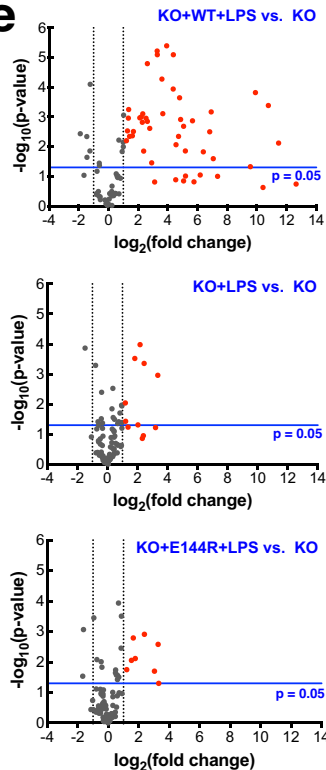
K63-linked poly-ubiquitylated interferon receptors (IFNAR1/2) are internalized and degraded via the lysosomal degradation pathway. The BRISC-SHMT2 complex is required for IFNAR1/2 deubiquitylation and receptor stabilization at the membrane. BRISC deubiquitylation of IFNAR1/2 receptors proceeds after SHMT2 displacement leading to sustained interferon signaling.

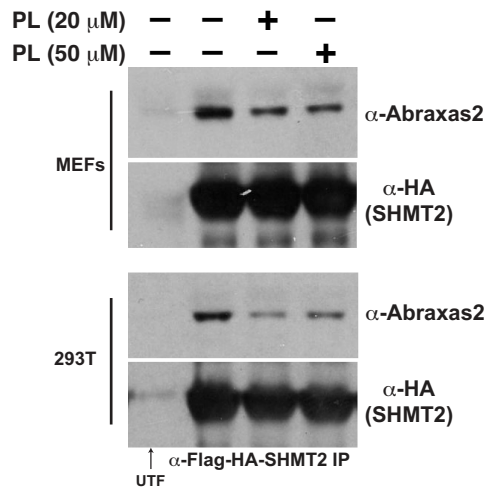
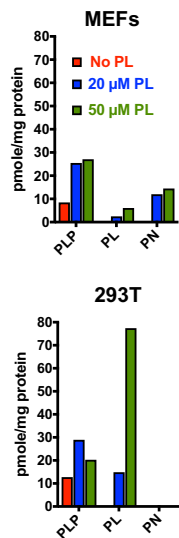
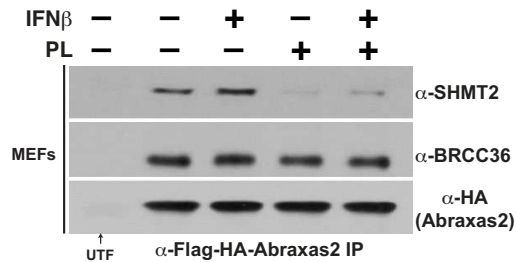
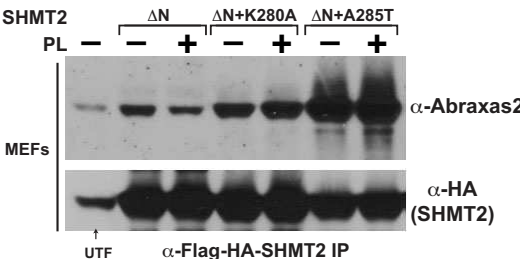
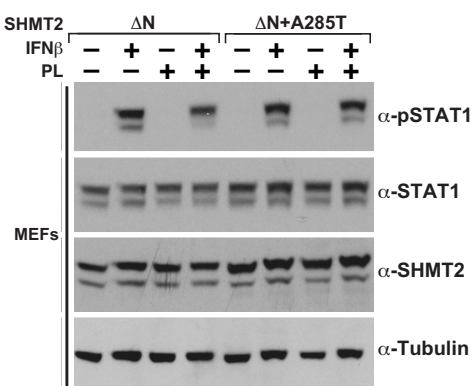
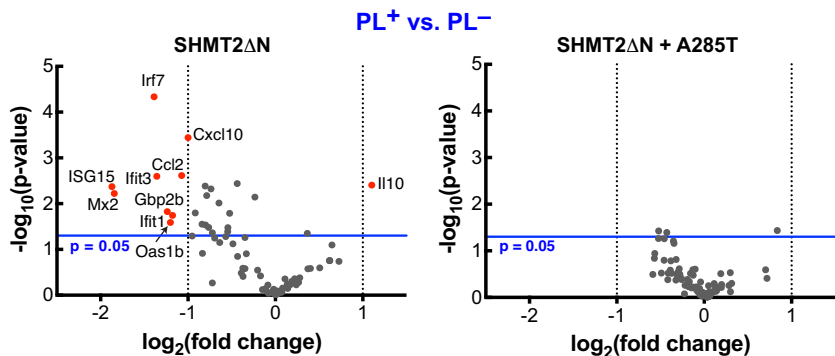
SHMT2 dimer-tetramer transition is regulated by pyridoxal-5'-phosphate (PLP) binding. Only an inactive SHMT2 dimer can interact with BRISC, whereas the active SHMT2 tetramer will sterically clash with BRCC36-Abraxas2 superdimer. Modulation of SHMT2 dimer-tetramer transition by PLP analogues or other binders could represent new ways to inhibit BRISC recruitment to IFNAR1/2 and reduction of interferon signaling.

**Extended Data Table 1.** Summary of data collection, image processing, model building, refinement and validation statistics.

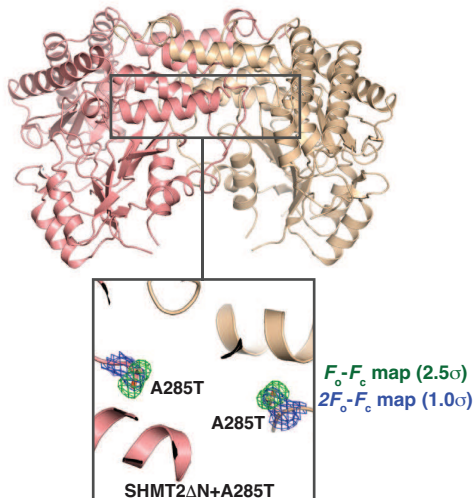


**a****b**

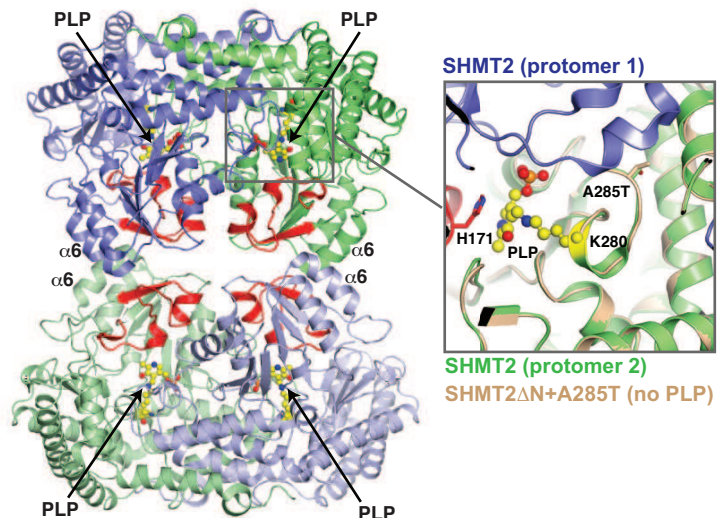
**a****b****c****d****e**

**a****b****c****d****e****f**

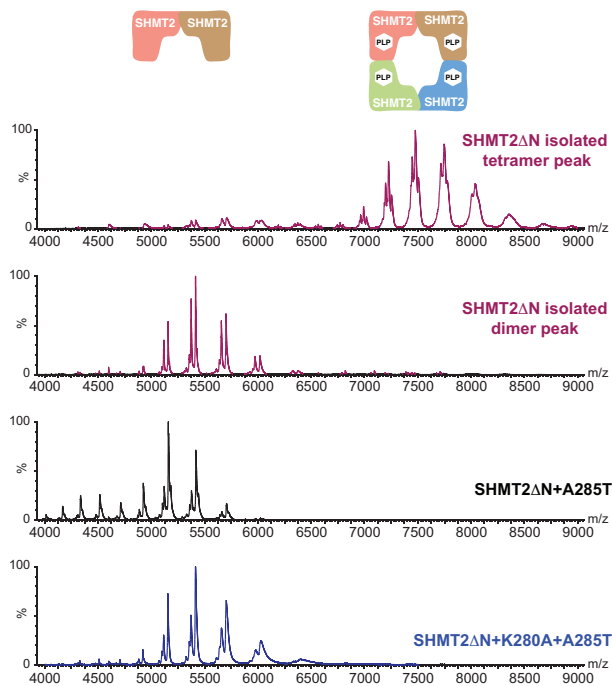
**a** SHMT2 dimer (no PLP)



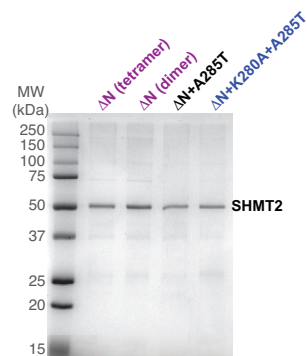
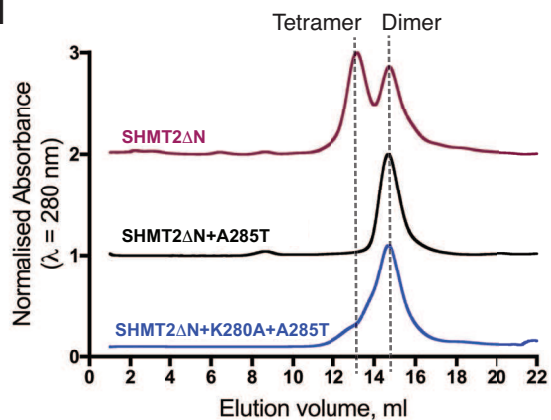
**b** SHMT2 tetramer (with PLP)



**c**

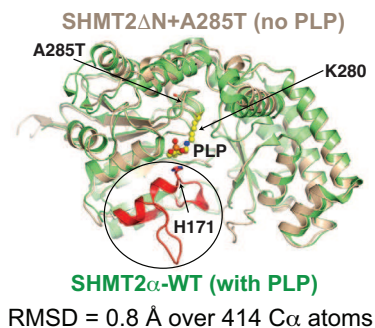


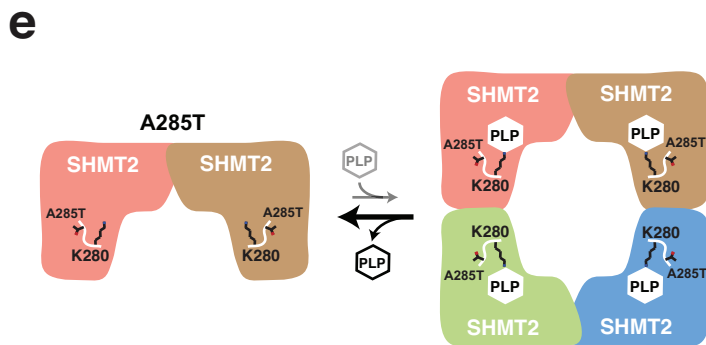
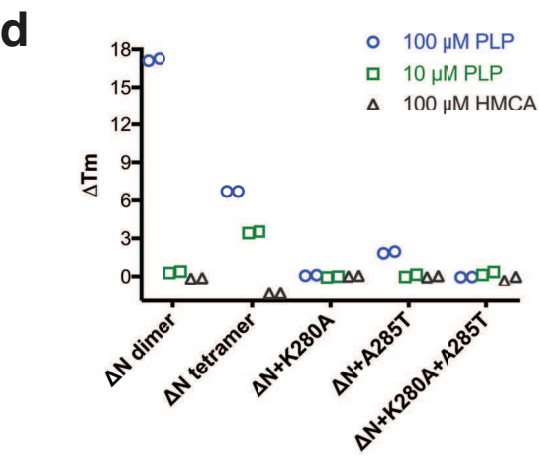
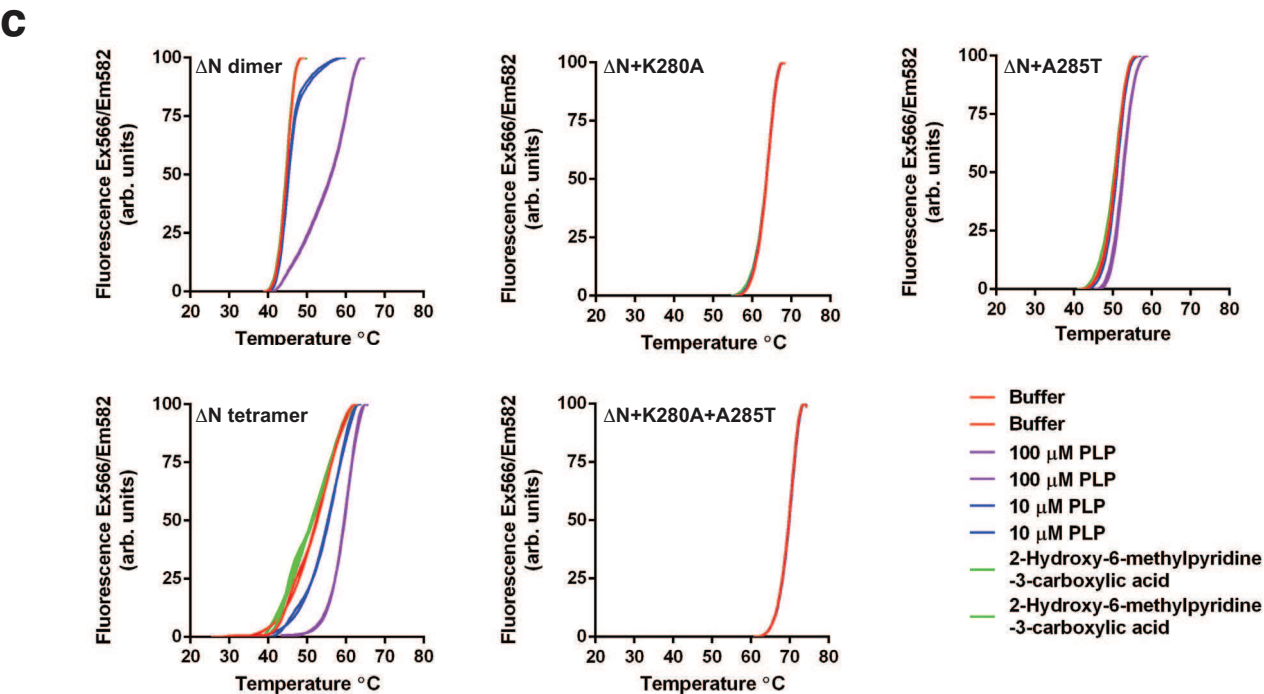
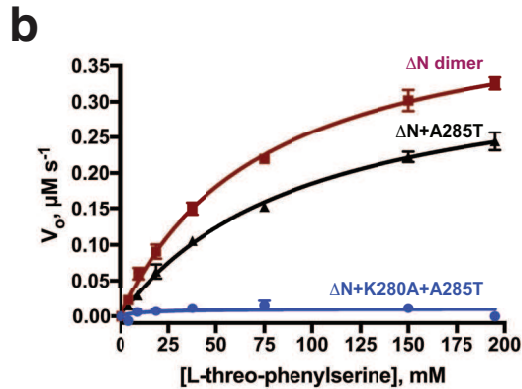
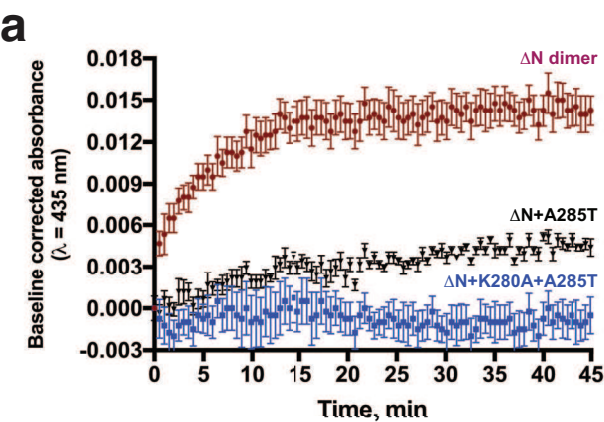
**d**



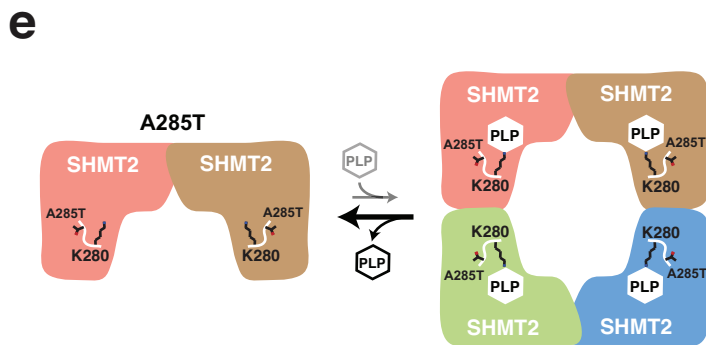
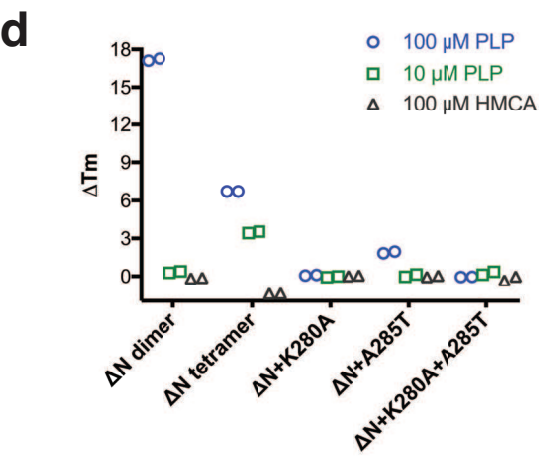
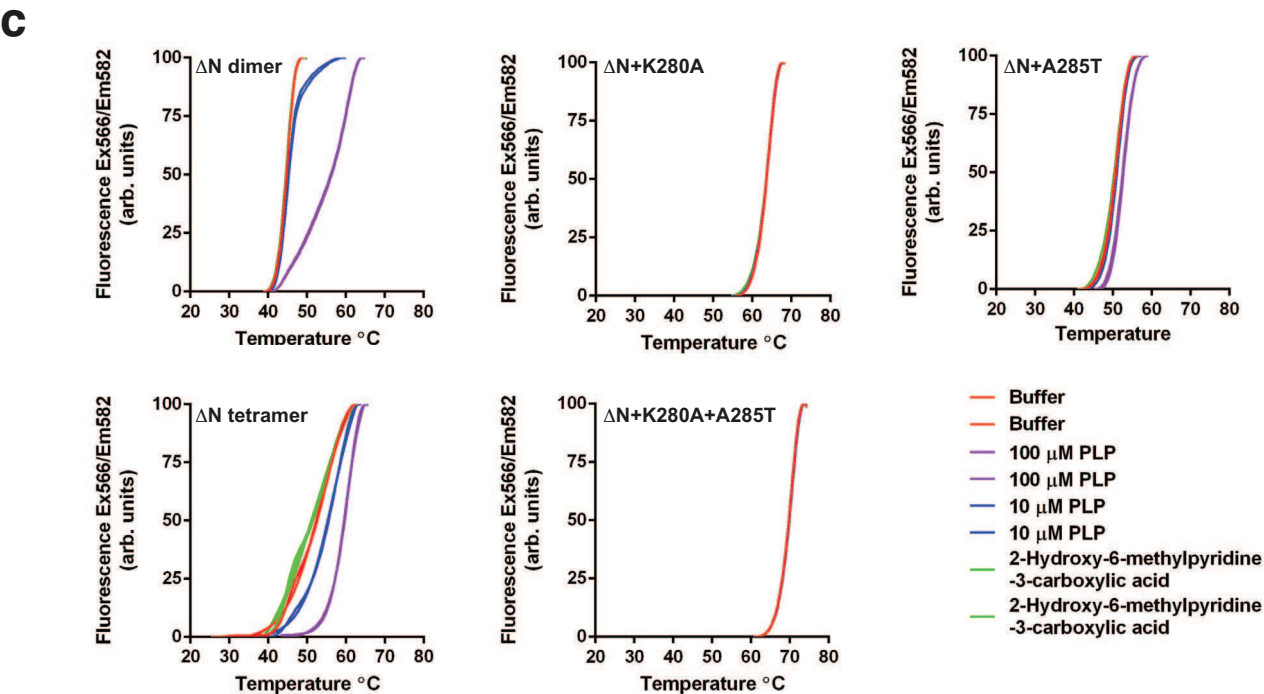
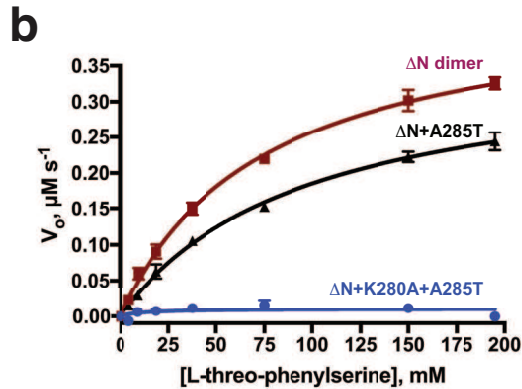
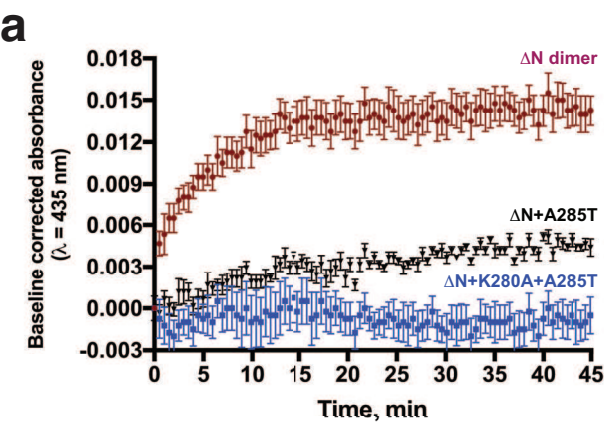
SHMT2 sample	Measured mass (Da)	Calculated mass (Da)		
		Monomer	Dimer	Tetramer + PLP <sub>4</sub>
$\Delta$ N tetramer peak	217185.0	54136.7	108273.4	<u>216775.9</u>
$\Delta$ N dimer peak	108286.0	54136.7	<u>108273.4</u>	216775.9
$\Delta$ N + A285T	108340.0	54166.7	<u>108333.4</u>	216896.0
$\Delta$ N + K280A + A285T	108160.0	54079.6	<u>108159.2</u>	216547.5

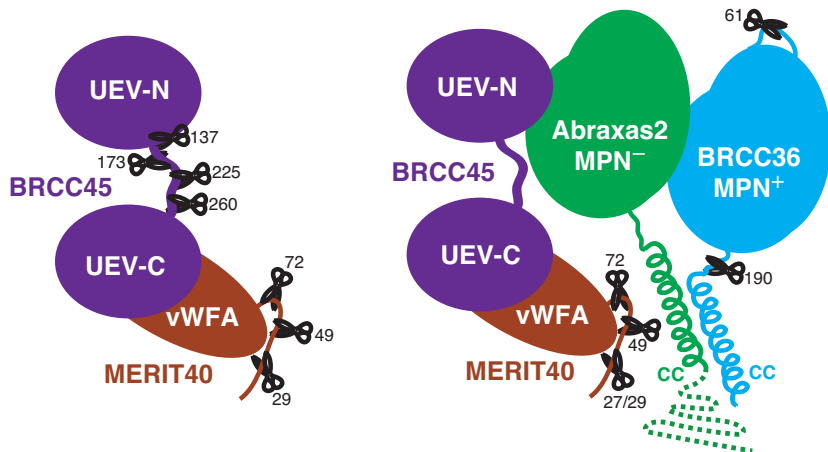
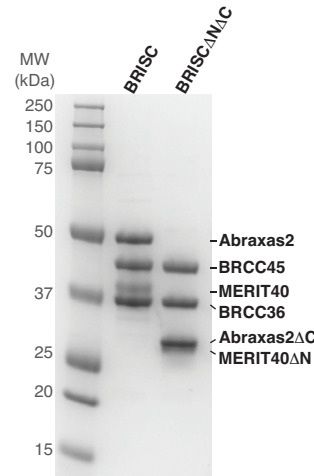
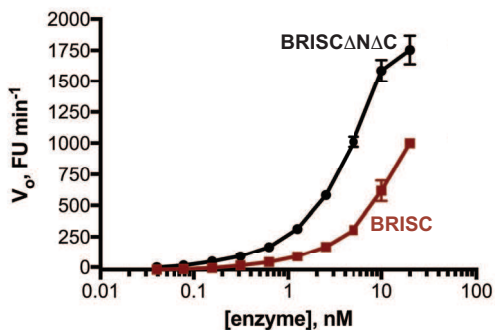
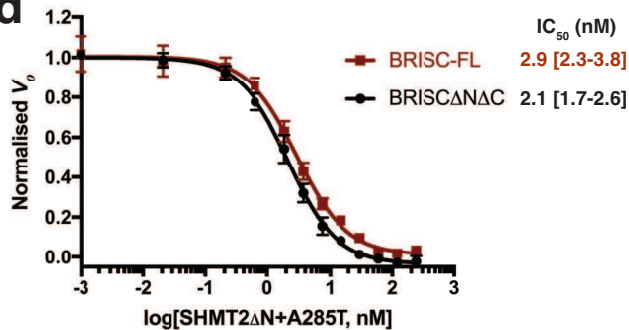
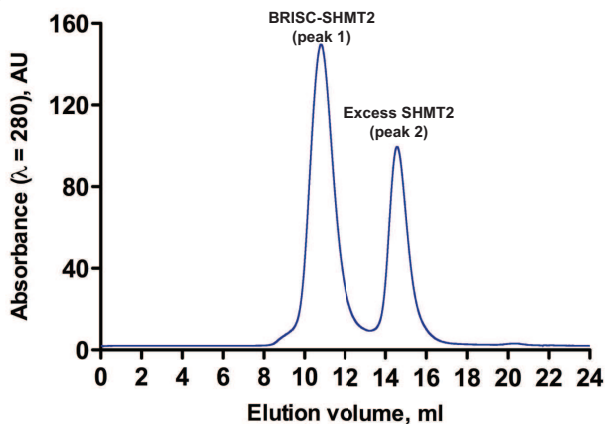
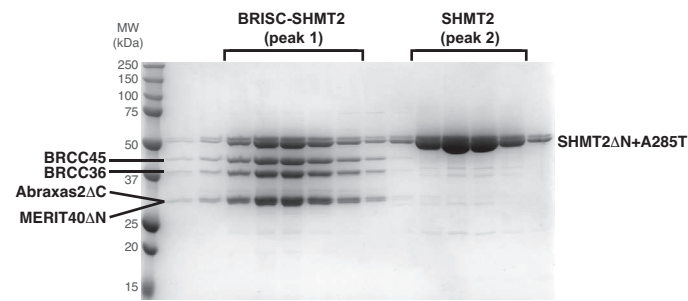
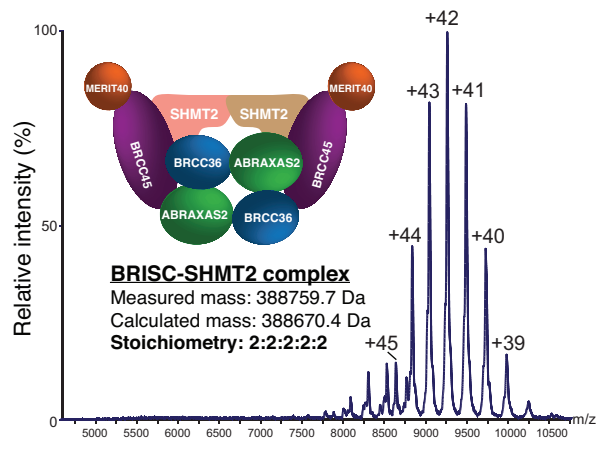
**e**



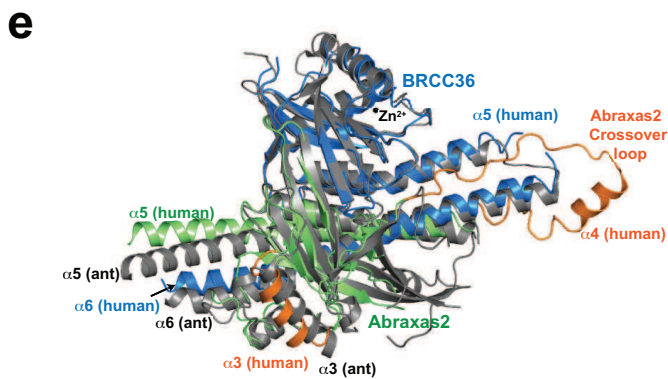
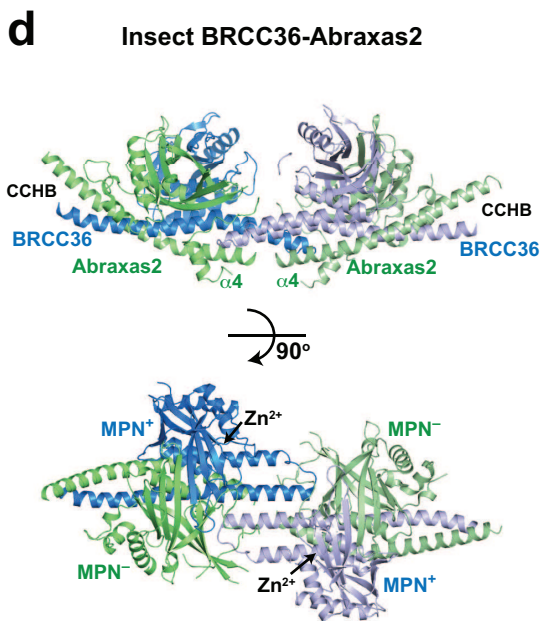
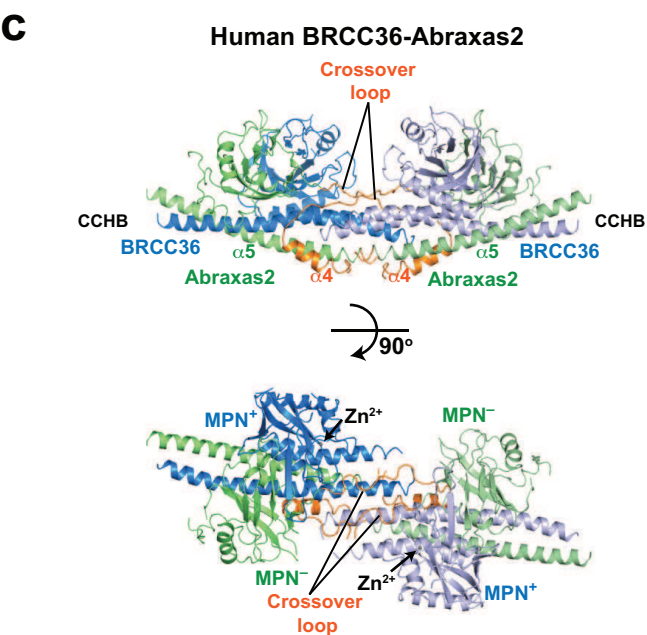
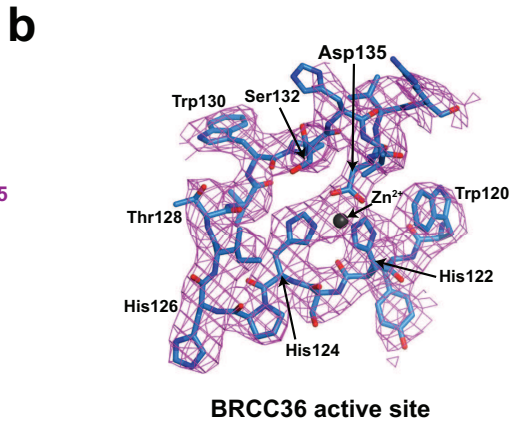
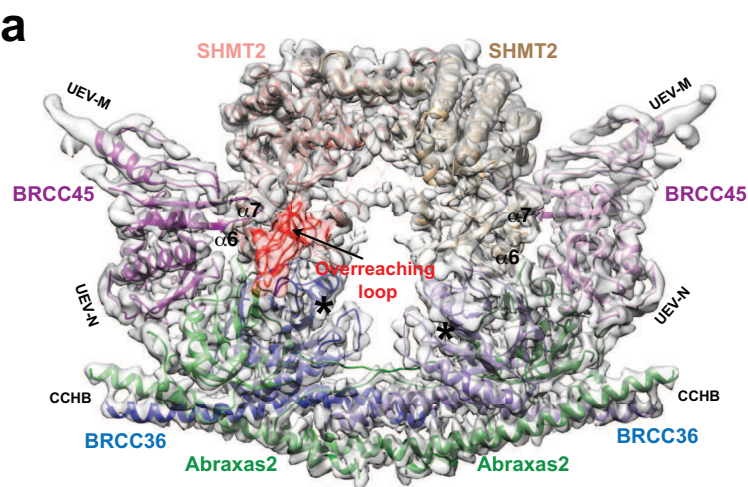


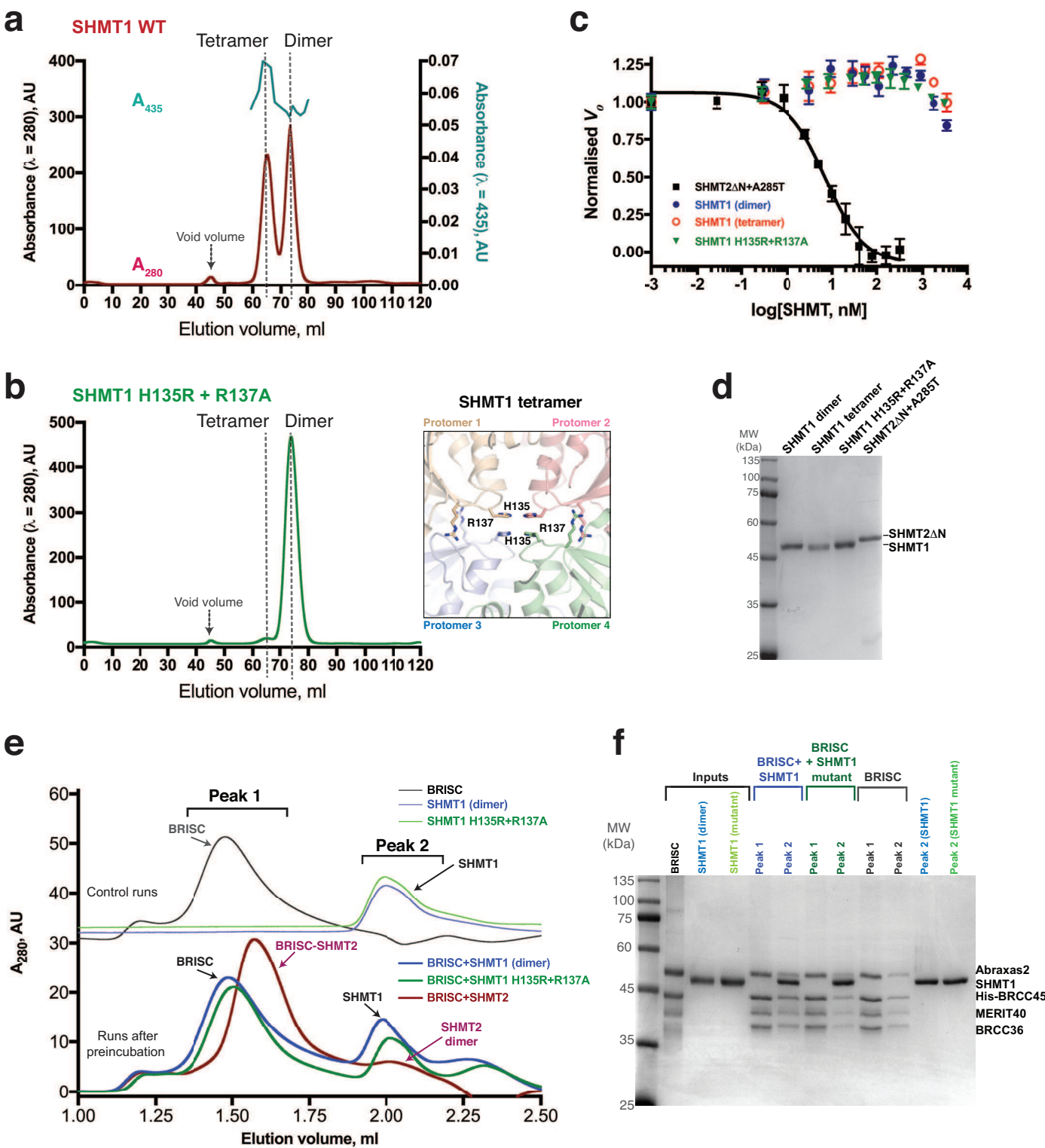


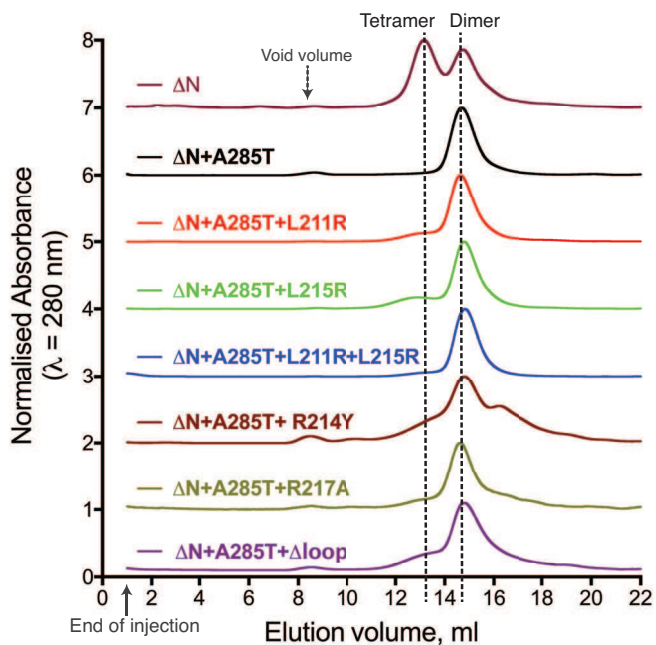
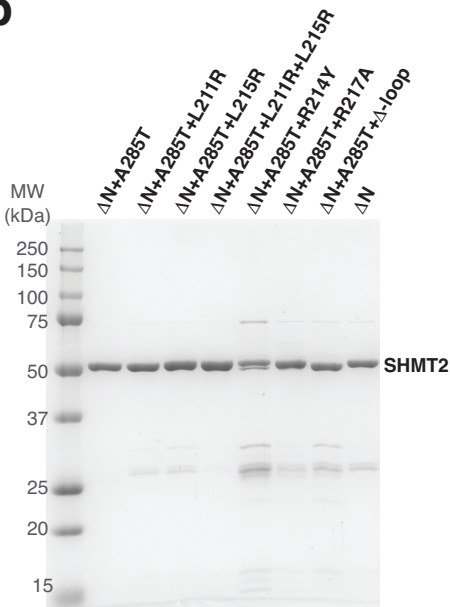
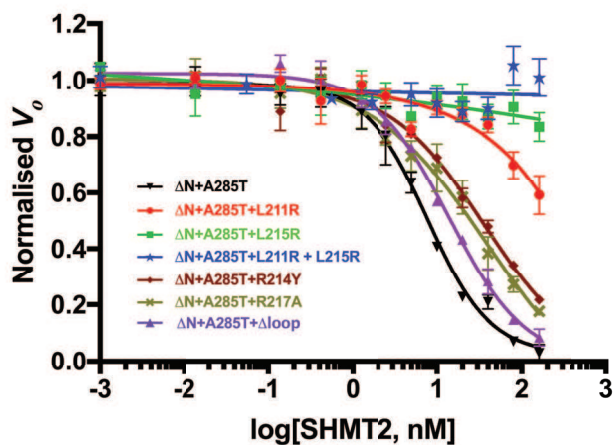
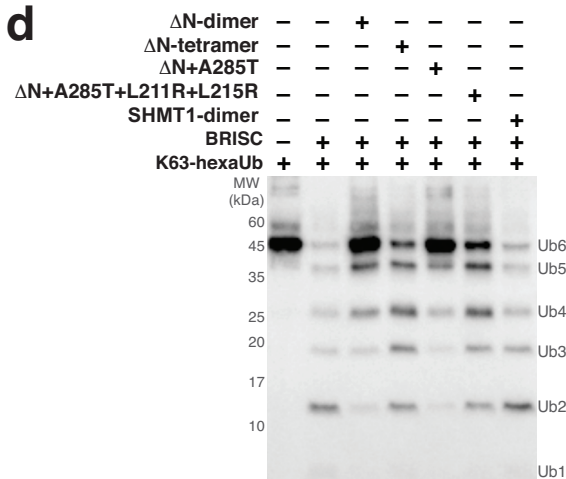
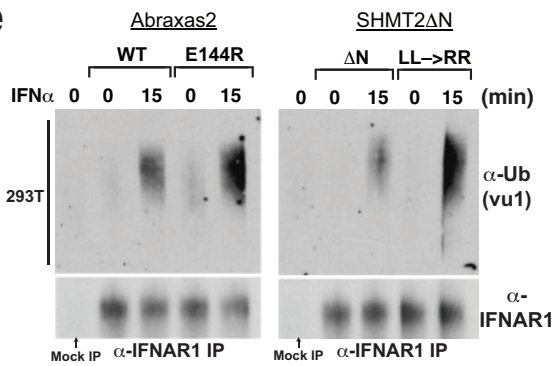
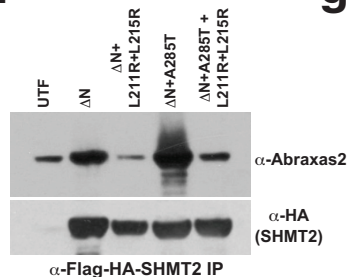
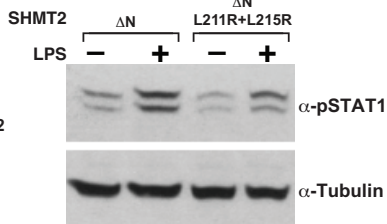


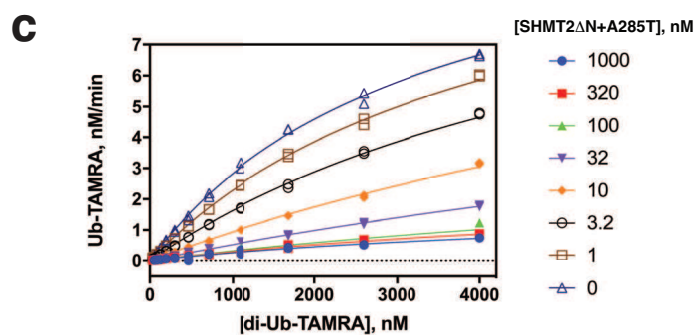
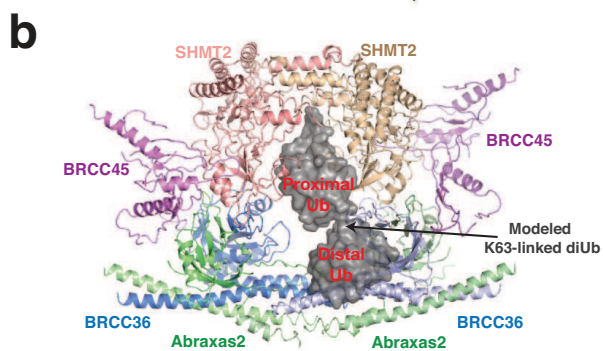
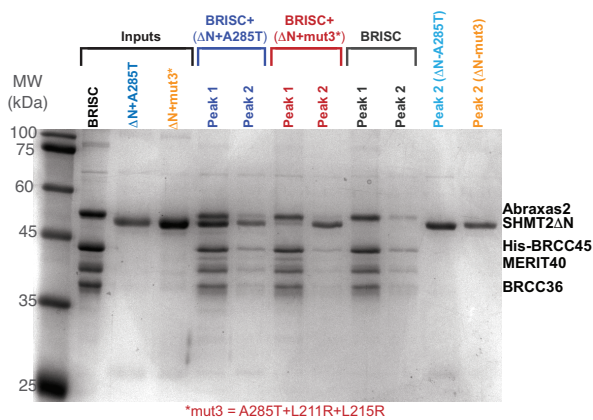
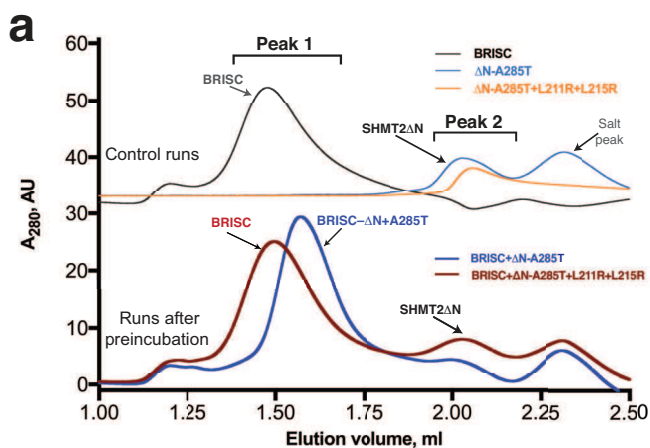
**a****b****c****d****e****f**



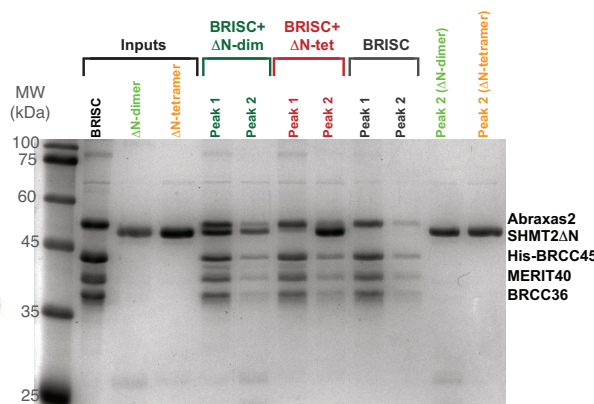
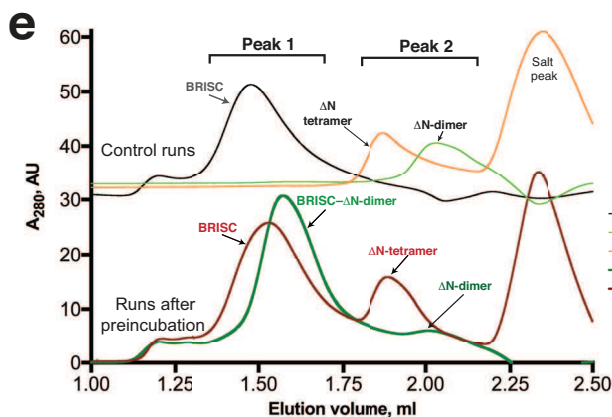
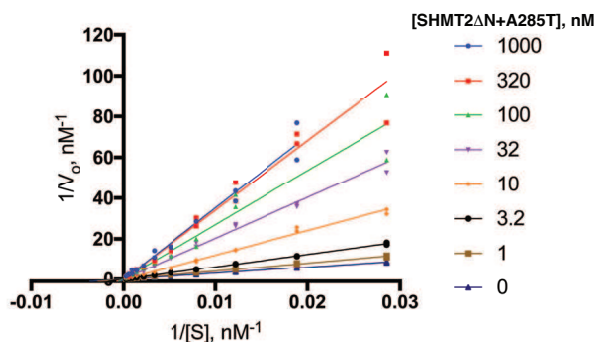
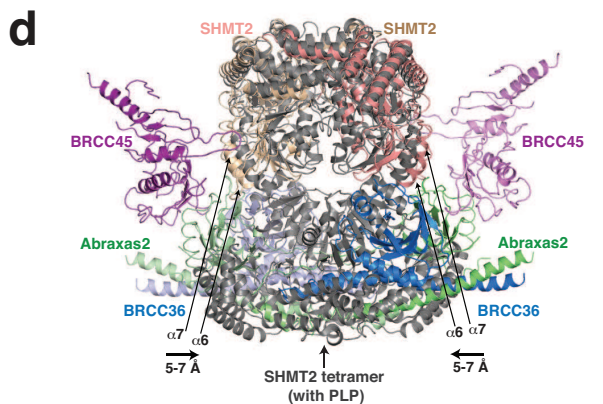


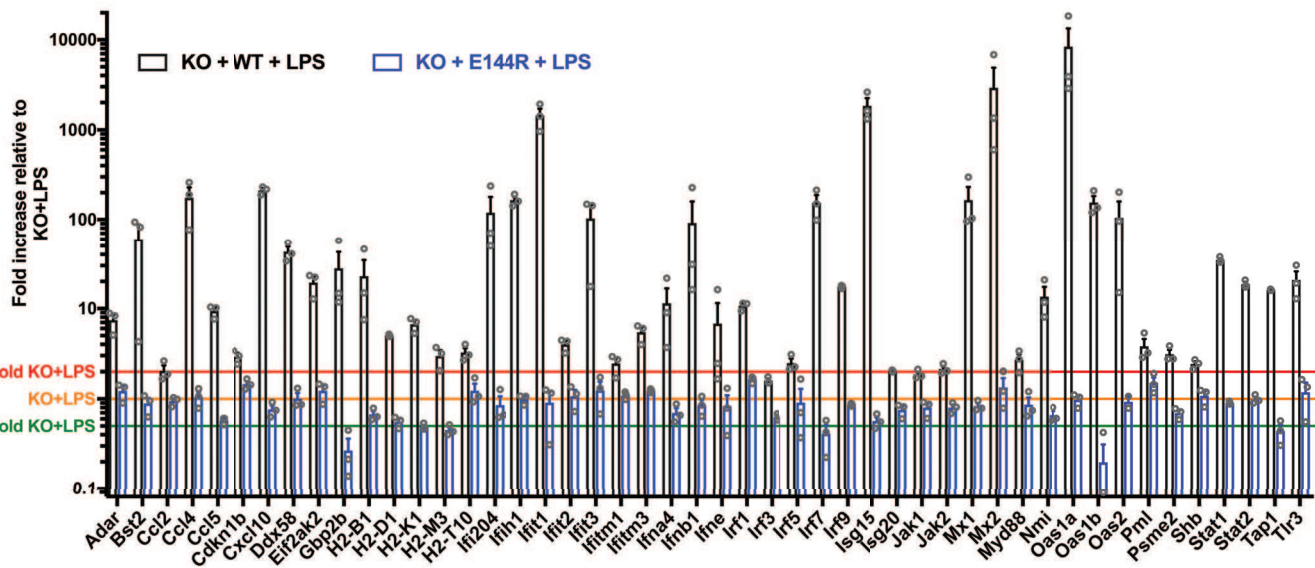
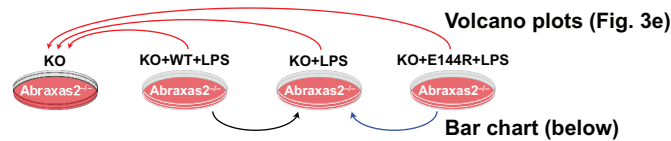
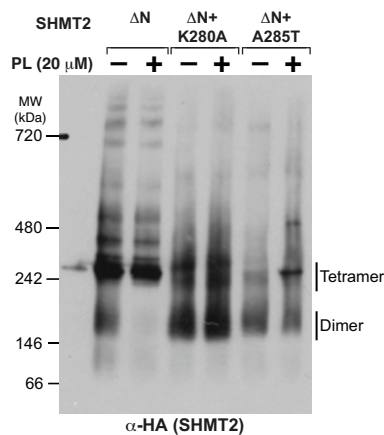
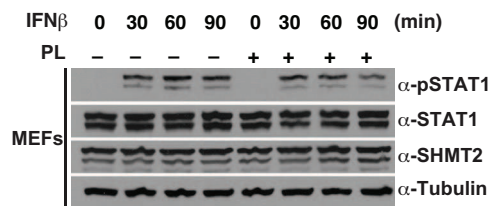
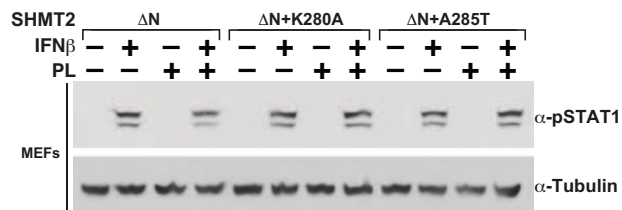
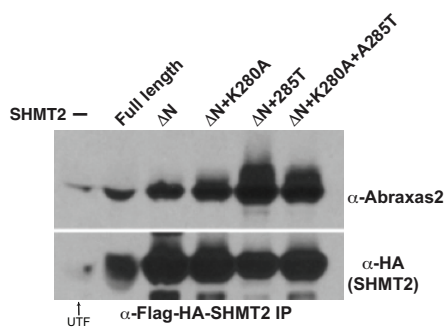
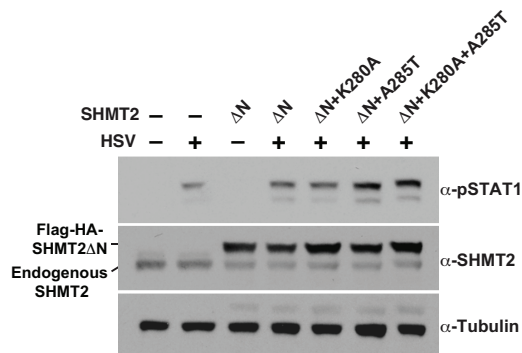


**a****b****c****d****e****f****g**



	1000	320	100	32	10	3.2	1	0
$V_{max}$ (nM/min)	1.893	2.638	3.842	8.595	~12.18	~12.18	~12.18	12.17
$K_m$ (nM)	6422	8219	11169	15485	11986	6465	4317	3302



**a****b****c****d****e****f**





	BRISCANAC-SHMT2 EMD-4759/EMD-4760, PDB 6R8F	BRISCANAC-SHMT2	BRISCANAC
<b>Staining</b>	None	Uranyl acetate	Uranyl acetate
<b>Data Collection</b>			
Microscope	FEI Titan KRIOS	FEI Tecnai F20	FEI Tecnai F20
Voltage (keV)	300	120	120
Detector	FEI Falcon III	FEI Ceta CMOS	FEI Ceta CMOS
Magnification	x75,000	x29,000	x29,000
Defocus range ( $\mu\text{m}$ )	-1.6 to -3.1		
Pixel size ( $\text{\AA}$ )	1.065	3.51	3.51
Electron dose ( $e^-/\text{\AA}^2$ )	Dataset 1: 95 Dataset 2: 83 Dataset 3: 86	15	15
Electron dose per frame ( $e^-/\text{\AA}^2$ )	1.2		
Exposure (sec)	2	1.5	1.5
No. of frames	Dataset 1: 79 Dataset 2: 70 Dataset 3: 71	1	1
No. of micrographs	7,494	222	218
<b>Data Processing</b>	<b>Complete dataset</b>	<b>2-arm dataset</b>	
Symmetry Point Group	C1	C2	
Final particle number	403,499	64,403	
Map resolution ( $\text{\AA}$ )	3.8	4.2	
FSC threshold	0.143	0.143	
Map resolution range ( $\text{\AA}$ )	3.5 – 10.0	3.9 – 11.5	
<b>Refinement</b>			
Initial models used (PDB code)	5CW3, 6DK3	5CW3, 6DK3	
Map sharpening B-factor ( $\text{\AA}^2$ )	-202	-182	
<b>Model Composition</b>			
Non-hydrogen atoms	15,810	15,810	
Protein residues	2,164	2,164	
Zinc ions	2	2	
<b>R.M.S.D from ideal geometry</b>			
Bonds lengths ( $\text{\AA}$ )	0.01	0.01	
Bond angles ( $^\circ$ )	1.07	1.00	
<b>Validation</b>			
Molprobit score	1.72 (88 <sup>th</sup> percentile)	1.80 (85 <sup>th</sup> percentile)	
Clashscore	3.53 (97 <sup>th</sup> percentile)	4.53 (95 <sup>th</sup> percentile)	
Poor rotamers (%)	0.00	0.27	
<b>Ramachandran plot statistics</b>			
Favored (%)	89.08	89.32	
Allowed (%)	10.92	10.68	
Disallowed (%)	0.00	0.00	